NIELS **B**OHR **I**NSTITUTE
(*Ice and Climate Group*)
FACULTY OF SCIENCE
UNIVERSITY OF COPENHAGEN
DENMARK

Master's thesis

Benoît Jean Régis BIZET

High resolution analysis of the NORTHGRIP ice core microstructures and fabrics: A detailed study of the Dansgaard-Oeschger events 1, 8 and 19.

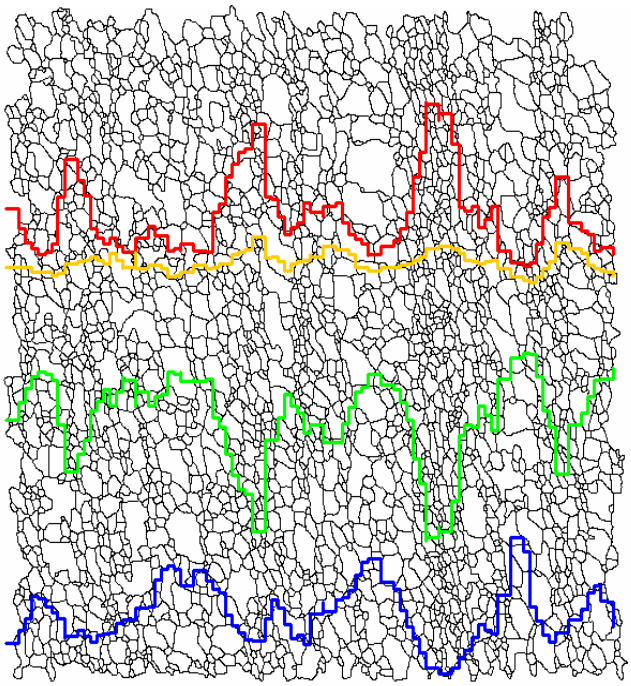

Academic advisor: Anders Svensson

Submitted: 12/06/06

Abstract

Analyse à haute résolution des microstructures et des fabrics de la carotte de glace NORTHGRIP: une étude détaillée des évènements Dansgaard-Oeschger 1, 8 et 19. Dans ce projet de maîtrise, dix-huit lames minces ont été coupées et préparées à partir de trois évènements Dansgaard-Oeschger choisis dans la carotte de glace NGRIP, afin d'analyser leurs crystaux. Les mesures effectuées sont divisées en deux groupes: les microstructures (taille et forme) et les fabrics (orientation) des crystaux. Les fabrics ont été mesurées à l'aide d'un *analyseur automatic d'axe-c*, et les microstructures sur trois programmes différents: *Image Pro*, *Virtual Basic* et une nouvelle extension de *Matlab*, la *Texture Toolbox*. Les échantillons ont été choisis sur trois changements climatiques rapides, dans le but d'analyser séparément la période chaude de la froide de chaque évènement. Donc, l'étude de la variation de la taille et de l'orientation des crystaux peut être réalisée à trois échelles différentes: la variation à court terme (échelle de la lame mince), la variation due au changement rapide de climat sous la dernière ère glacière et la variation à long terme due aux changements d'écoulement et de température de la glace.
Les principaux résultats ont été ensuite corrélés avec des mesures à haute résolution déjà éxistantes, comme la stratigraphie visuelle et le C.F.A. (Analyse à Flux Continu). De par ces observations, il apparaît que les résultats obtenus sont en accord avec ceux des précédents projets réalisés sur les carottes de glace de GRIP (Thorsteinsson *et al.*, 1997) et de NGRIP (Wang *et al.*, 2002, Svensson *et al.*, 2003a and 2003b). De plus, les tailles et les orientations des crystaux ont révélé des variations simultanées à l'échelle saisonière pour les évènements D.O. 1 et 8, mais aussi à l'échelle de la lame mince pour l'évènement D.O. 19, ce qui représente une nouvelle observation dans l'analyse des crystaux de glace.

High resolution analysis of the NORTHGRIP ice core microstructures and fabrics: A detailed study of the Dansgaard-Oeschger events 1, 8 and 19. In this master project, eighteen vertical thin sections have been sampled/cut and prepared from three selected Dansgaard-Oeschger events (D.O. 1, 8 and 19) in the NGRIP ice core, in order to analyze their ice crystals. The performed measurements are separated in two main groups: the microstructures (size and shape) and the fabrics (orientation) of the crystals. The fabrics have been measured on an *automatic c-axis analyzer*, and the microstructures on three different computer programs: *Image Pro*, *Virtual Basic* and a new *Matlab* toolbox, the *Texture Toolbox*. The

samples have been chosen over three abrupt climatic changes in order to analyze the warm and the cold period of each event separately. Therefore, the study of the variation in crystals size and orientation can be performed at three different time scales: the short term variation (thin section scale), the variation due to the rapid climate change under the ice age and the long time variation due to ice flowing and temperature changes.
The main results have been correlated to already existing high resolution measurements such as the visual stratigraphy and the C.F.A. (Continuous Flow Analysis). From these observations, it appeared that the extracted results agreed with the previous works performed on the GRIP (Thorsteinsson *et al.*, 1997) and the NGRIP ice cores (Wang *et al.*, 2002, Svensson *et al.*, 2003a and 2003b). Moreover, the crystal sizes and orientations have been showing simultaneous variations at the seasonal scale for the upper events (D.O. 1 and 8), but also at the thin section scale for the lowest event (D.O. 19), which represents a new observation in ice crystal analysis.

Preface

First, I would like to thanks Anders Svensson, my supervisor, for his engagement in my project. His experience and his knowledge on ice crystals, together with his helpful and inspiring assistance and supervision have been of great importance, and worked as a motivating factor. I am indebted to Gaël Durand, for his patience and his program, which made the statistical analysis more precise.Finally, I would like to thank Rémi Chalmas, who helped me to get to the right storing box in the huge freezer of the H.C. Ørsted institute.

Three chosen Dansgaard-Oeschger events, the D.O. 1, D.O. 8 and D.O. 19, representing rapid climate changes going from a cold period to a warmer one are going to be studied through the 18 ice samples which have been cut from the North Greenland Ice Core Project (NGRIP)[Dahl-Jensen et al., 2002] and [North Greenland Ice Core Project Members, 2004]. The complete analysis has been performed at Rockefeller, Ice and Climate Group, Niels Bohr Institute (NBI), University of Copenhagen. The practical work (thin sections and scanning) has been done in the freezer where the cores are stored, while the corrections on the thin sections scans, determination of the crystal borders together with the elimination of the eventual cracks have been done by using different softwares like *Image Pro*, *Investigator* and *Virtual Basic*. The statistical analysis has been performed by using a new program *Texture Toolbox*, written by Gaël Durand as a work of his post doctorate.

I started this project in November 2004, by collecting the ice samples and by preparing 18 thin sections. At the end of November 2004, all the thin sections were ready and digitalized by scanning. A break of six months followed this first phase due to a study travel to Svalbard, where I took my last master courses. I continued to work on the project from July 2005, alternating a week at the university and a week at work, because of the missing state subventions. Since the beginning of 2006, I worked full-time on the project.

Contents

Chapter 1

Introduction

The following chapter presents a short introduction to the two main ice sheets in the world, Antarctica and Greenland. Since the 1950's, both places have been hosting ice core drilling projects, in order to collect some important paleoclimatic information. The North GReenland Ice core Project (NGRIP) is one of the most recent drilling program, and is considered as one of the most reliable source of data. NGRIP is located on the top of a ridge, at about 300 kilometers north of the Summit site (Central Greenland). Since all the collected and analyzed data in this thesis come from the NGRIP ice core, the coming sections will essentially deal with the NGRIP ice core, its properties and its characteristics such as the chemical composition of the ice or its physics.

1.1 Ice Sheets and ice cores history

In the middle of the fifties (1956), the ice core pioneers extracted a 400 meters ice core at Site 2 (NW-Greenland). In 1966, the first core to reach bedrock was drilled at Camp Century (NW-Greenland), containing climatic information about the past 100000 years. At the same time, ice drilling projects also emerged in Antarctica, with the first core at Byrd Station (West Antarctica, 1968). Since then, the two ice sheet have been hosting many other drilling projects such as the Dye 3 project (Southern Greenland, 1981), the GReenland Ice core Project (GRIP)(Summit, 1992), the GISP2 project (Summit, 1993) and the North GReenland Ice Core Project NGRIP (Central Greenland, 2002) . Meanwhile, Antarctica provided, among others, some cores at Dome C (South-Eastern Antarctica, 1978), at Vostok (Eastern Antarctica, 1995) and lately, at Dome C again, with the European Project for Ice Coring in Antarctica (EPICA), which in 2005 extracted a core of more than 3000

meters that covers about 800000 years of climate history, containing 8 glacials . All the cited drilling projects are shown on the two maps of the figure 1.1.

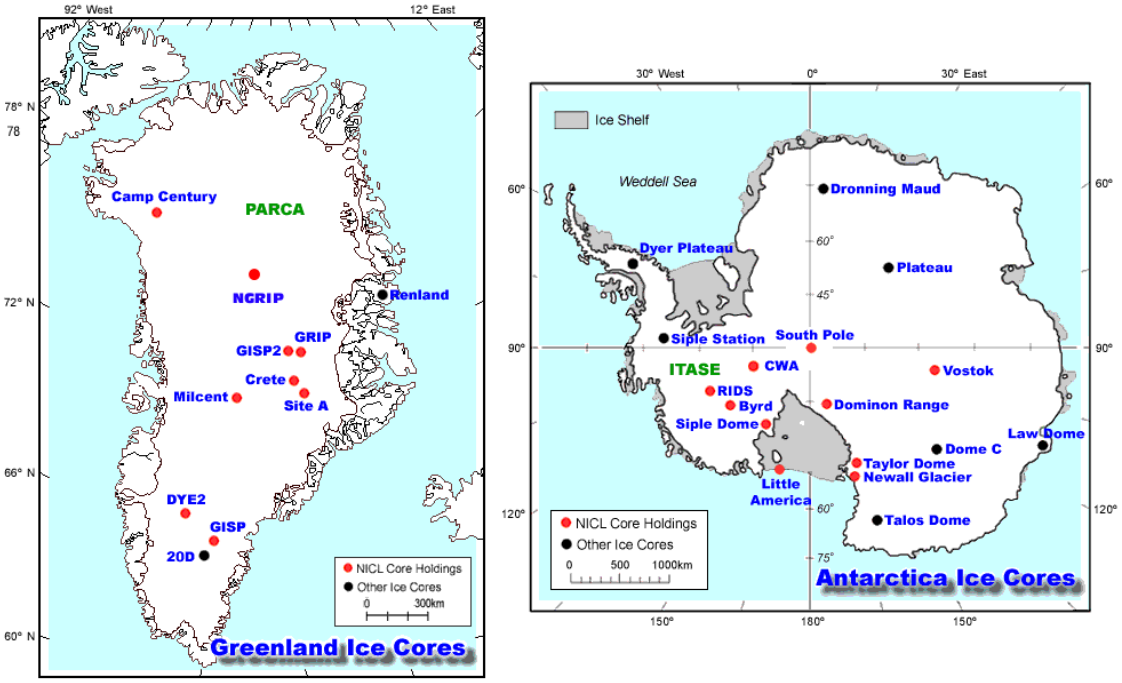

Figure 1.1: *This figure shows two maps, on the left, a map of Greenland, on the right a map of Antarctica, presenting their respective drilling sites (taken from National Ice Core Laboratory home page: http://nicl-smo.unh.edu/index.html).*

Ice sheets are made of ice, resulting from snow. The transformation from snow to ice passes through a stage called firn. Snow generally defines an unchanged material while firn represents an intermediate stage. The firn is the wetted snow that has survived one summer without being transformed to ice [Paterson, 1994]. The accumulation of new snow grains on the top of the firn makes it sink further down to the already existing ice and let the firn's density increase. Typically, the firn becomes ice at a density of 830 kgm^{-3} [Paterson, 1994]. Consequently, the annual snow deposition can be tracked back, to enable a dating of the ice core. It is though important to notice that the annual layers get thinner with depth, due to the pressure of the overlaying ice, and that they can get disturbed either by ice flow or by bedrock topography (or both)[Dahl-Jensen et al., 2002]. The main flow properties of an ice sheet are well illustrated on figure 1.2. The central part

of the figure represents the top of the ice sheet (also called the summit), from where ice is sinking and flowing. The compaction of the ice results in the thinning of the layers as it appears on the central part of the schema. The vector V_x stands for the horizontal flow velocity of the ice, which is decreasing with depth. Some complementary explanation concerning the flowing and thinning of the ice, as well as the processes that govern the transformation of snow to ice will be given in the coming chapters.

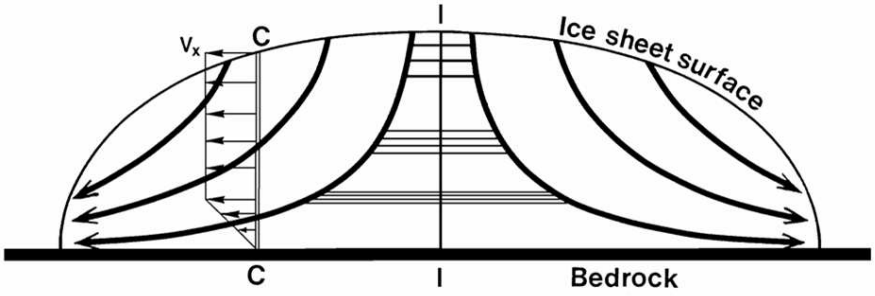

Figure 1.2: *Schematized ice sheet resuming most of the physical processes of the sheet (flow of the ice resulting in the thinning of the annual layers with depth, ice flowing...).*

1.2 Paleoclimatic information from ice cores

Snow, firn and ice from ice cores provide important paleoclimatic information. In the nature, water is composed of three important isotopic components, $H_2{}^{16}O$, $HD^{16}O$ and $H_2{}^{18}O$. A continuous analysis of the $\delta^{18}O$ ratio for an ice core reflects the annual precipitations on the site. For any sample, the $\delta^{18}O$ ratio can be calculated (using the equation 1.1) [Craig, 1961] to define its relative deviation from the standard composition (SMOW: Standard Mean Ocean Water).

$$\delta^{18}O = \frac{R_{Sample} - R_{SMOW}}{R_{SMOW}} \times 1000, \tag{1.1}$$

where R_{Sample} and R_{SMOW} respectively represent the ratio between ^{18}O and ^{16}O for the sample, and for the reference standard composition. The heavy ^{18}O isotope has a slightly lower water pressure than the ^{16}O, thus, the heavy ^{18}O evaporates less rapidly and condenses readily from the vapor. Consequently, the isotopic composition of the water changes during cycles of evaporation and condensation. Because evaporation and condensation always

reduce the amount of the heavy isotope, the $\delta^{18}O$ ratio of precipitation always appears to be negative (see figure 1.3). Water pressure is closely related to temperatures, therefore, annual averages of the $\delta^{18}O$ ratio are highly correlated with mean annual temperatures. Moreover, ice cores provide important information about the chemistry of the atmosphere. Air bubbles, trapped in the ice reflect the atmospheric composition at the time of their formation. Because the bubbles are located in the firn/ice transition, the air is younger than the surrounding ice [Paterson, 1994]. The chemistry composition of the ice cores can be analyzed by using the Continuous Flow Analysis (CFA), which enable the detection of the concentration of different ions; among them, Ca^{2+}, Na^{+}, $NH_4{}^{+}$, $SO_4{}^{2-}$ and $NO_3{}^{-}$. Each of these ions has a known origin, the calcium comes from the terrestrial erosion, the sulfate and the nitrate from volcanic activity and the sodium from sea-salt. These concentrations, together with an analysis of the dust content will enable a counting of the annual layers as they all have seasonal variations. But the most powerful tool that enables the counting of the annual layers is the visual stratigraphy. The seasons are represented by some cloudy bands (spring and summer) and bright bands (autumn and winter)[Svensson et al., 2005]. Finally, preserved ash layers appear on the ice cores. They represent a powerful correlation tool as they can be dated if the volcanic eruption is known from other places in the world.

1.2.1 The Dansgaard-Oeschger Events (D.O. events)

To explain the Dansgaard-Oeschger events, it is necessary to distinguish different definitions such as *glacials*, *interglacials stadials* and *interstadials*. The glacials are commonly known as the ice-age. During the Earth's recent climate history, many glacials have been recognized (essentially from deep-sea cores but also from the latest ice core from Dome C). Each of these glacials is followed by a warmer period, the interglacial, such as the Holocen period we are now in. It is now easier to understand the D.O. events; during the glacials, periods of abrupt temperature shifts occur, going from a cold to a warmer period in a relatively short lapse of time. The cold state is known as the stadial, and the warm one as the interstadial [Dansgaard et al., 1993]. These sudden shifts appear in the isotopic record ($\delta^{18}O$) of all the deep ice cores from Greenland (figure 1.3). Schulz (2002) noticed a recurrence on these D.O. events, with a prominent 1470-years spectral peak. His research has though been done on the GISP2 ice core, but since the D.O. events are correlated with the other cores, the same recurrence should be expected on GRIP or NGRIP.

1.3 The North GReenland Ice Core Project (NGRIP)

The North GReenland Ice Core Project (NGRIP) site is located at 75.10°N and 42.32°W, at an elevation of 2917 m (figure 1.1). The NGRIP drilling started in 1996, and reached bedrock in July 2003. The total ice core length is 3091 m. The average temperature at the site is -32°C and the accumulation rate is 0.5 m snow/year or 0.2 m ice/year. NGRIP is the most recent Greenland ice core and has been drilled after GRIP (GReenland Ice Core Project), to try to get paleoclimatic information about the last interglacial period, Eem. NGRIP isotopic record is continuous from Holocene to the end of Eem. It enables the identification of 23 rapid and warm climatic changes,

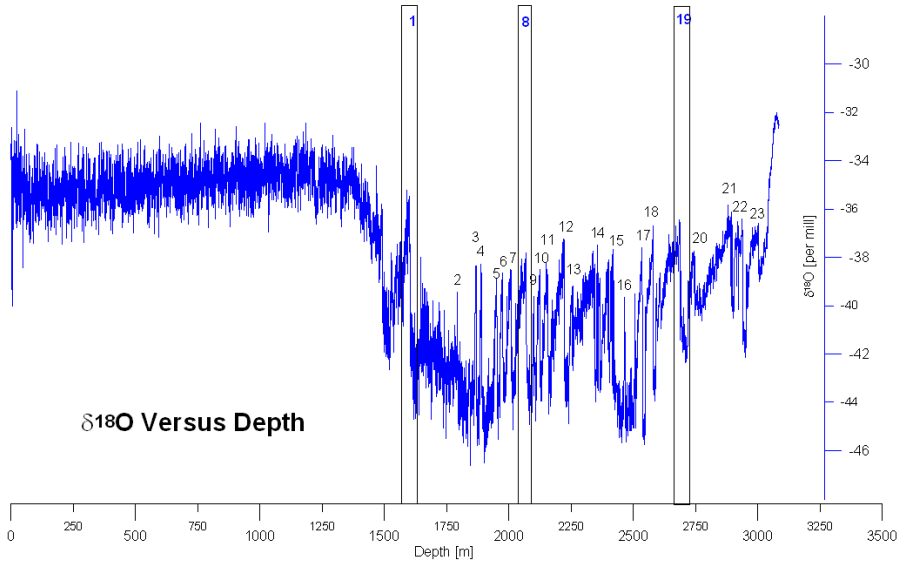

Figure 1.3: *$\delta^{18}O$ versus Depth, showing the 23 recurrent Dansgaard-Oeschger events. The framed events are the ones this thesis is concentrated on, the D.O. 1 (Bølling), the D.O. 8 and the D.O. 19.*

the Dansgaard-Oeschger (D.O.) events between the two interglacials, Eem and Holocene. The counting of the annual layers (with the help of the visual stratigraphy and the chemical components referred in the section 1.2) on the GRIP and NGRIP ice cores enabled to track time back to about 60000 years. The dating of the rest of both cores has been performed by modeling the annual layers thinning resulting from the flowing properties of the ice sheet [Johnsen, 2002]. This method lead to an approximate age of 250000 years at the bottom of the GRIP core ($\approx$ 3000 m) and 120000 at the bottom

of the NGRIP one (3091 m). This difference in age implies a difference in the annual layers thickness. Since the two cores are almost as long but represent a different time interval, the annual layers in GRIP must be thinner than the ones of NGRIP (at least toward the bottom). The next paragraph will try to picture this difference in resolution.

1.3.1 NGRIP vs. GRIP

The NGRIP ice core, like the GRIP or other ones, enables continuous measurements of different parameters such as the δ^{18}O, as plotted on figure 1.3. The main advantage of the NGRIP ice core, compared to the GRIP one is the high resolution of the climatic events, because NGRIP and GRIP have different physical properties. The stratigraphy of the NGRIP ice core is better conserved (less disturbed) than the one of GRIP (figure 1.4), due to the bottom topography. The bedrock is flat at NGRIP, while it is uneven at GRIP. Therefore, together with improvements of the technology, the results

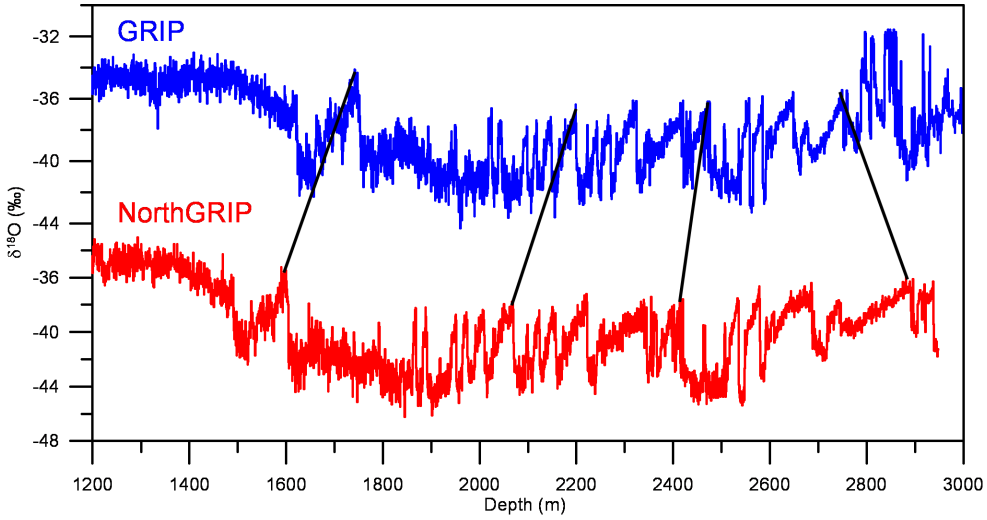

Figure 1.4: *$\delta^{18}O$ GRIP vs. NGRIP. The four compared events (black lines) reveal the difference in resolution of the two cores. The deeper, the greater the difference is.*

provided by the analysis of the NGRIP ice core seem to be more suitable for seasonal variation studies. There is though an inconvenient at the NGRIP site, in the fact that the bottom of the core is melted, it means that some precious paleoclimatic information gets lost. The melting is in the range of one centimeter per year, which correspond more or less to one/two years of climate history. The annual layers at that depth are estimated to be reduce

to about 0.5 centimeter (due to many parameters such as compression and ice flowing) [Johnsen, 2002].

1.4 This thesis

The main purpose of this experimental master thesis is to try to get an understanding of the processes that control the ice crystals size and orientation changes on different time scales. A correlation between the obtained data and the existing high resolution physical and chemical properties of the ice should give some useful information such as the relation between the impurities content and the grain size, the seasonal climatic information or the effect of the flow on the grains. A further comparison with some previous measurements made on other ice cores, essentially on GRIP (Thorsteinsson 1996 and Hansen, 2001) will be used to discuss the obtained results.
The coming chapter will give a general introduction to the ice formation and its physical properties in order to understand the changes in the crystal lattice. The presentation of my measurements methods on the NGRIP ice core will then follow in chapter 3. Chapter 4 will introduce the microstructural and fabric measurements that can be performed on ice crystals. Finally, the last chapter will present my results together with their interpretation and some comparisons to some of the previous works done on ice crystals, [Thorsteinsson, 1996], [Hansen, 2001] and [Wang et al., 2002].

Chapter 2

Ice and ice crystals physical properties

As mentioned before, snow is turning to ice through different processes. When snow is transformed into ice, its physical properties are changed. The following chapter gives an introduction to the ice formation and its physical properties at the single crystal and at the polycrystal scale.

2.1 Ice formation: from snow to ice

On glaciers and ice sheets, two type of snow must be distinguished, the wet snow and the dry snow. The wet snow is usually located on the borders of the ice sheets or glaciers and the dry snow at the middle of these. These two types of snow led to the distinction of two main zones, the wet zone and the dry zone. The zonation was first proposed by Ahlman (1935) and further developed by Benson (1961) and Müller (1962) . The wet zone is constituted of firn with ice layers and lenses that overlays snow, whereas the dry snow is only snow [Paterson, 1994]. The two zones lead to different mechanisms of metamorphism; since the work of this thesis is concentrated on ice cores drilled on the dry zone (NGRIP and GRIP), only a description of the processes on the dry zone will be presented.
In the dry zone, no melting occurs, which means that snow turns into ice according to the vapor pressure gradients. Vapor diffuses from high vapor pressure to low vapor pressure. The pressure gradients are controlled by temperature gradients, that are controlled by the diurnal and seasonal oscillations of the air temperature. Water vapor from the warmer snow pack will diffuse to the colder snow pack. It will then condense and lead to crystal growth. Another controlling parameter of snow metamorphism is the

radius of curvature of the snow/ice crystals. Vapor pressure is greater on crystal with small radii of curvature, thus the vapor pressure decreases with increasing radii of curvature.

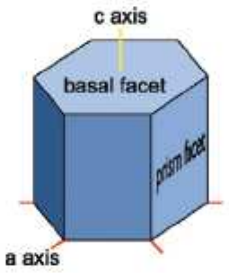

Figure 2.1: *Ice in the hexagonal prism form, showing the principal crystal axes and facets: 6 prism facets, 2 basal facets and 4 main axes, 3 a-axis that are parallel to the basal facet and 1 c-axis that is parallel to the prism facet. From [Libbrecht, 2005].*

2.2 Structure of ice

Ice is a polycrystalline material, which means that it is composed of aggregates of crystals . To understand better the deformation of the polycrystalline ice, an approach to the deformation of a single ice crystal is be presented in this section.
The normal form of ice is generally represented by an hexagonal crystal structure, which grows to an hexagonal prism (figure 2.1). This crystal type is usually called the ice I_h, where crystals are growing along the 4 axes shown and named on figure 2.1. The c-axis is also known as the optical axis and will be subject to many analysis in the coming chapters, because it is this axis that is used to determine the orientation of the single crystals. The crystal structure of ice shows oxygen atoms arranged in layers of hexagonal rings. The atoms are alternating in an upper and lower plane to produce a two planes structure, figure 2.2. Therefore, ice crystal can appear either in

plate or in columns, depending on the rate of growth of the basal and prism facets, figure 2.1.

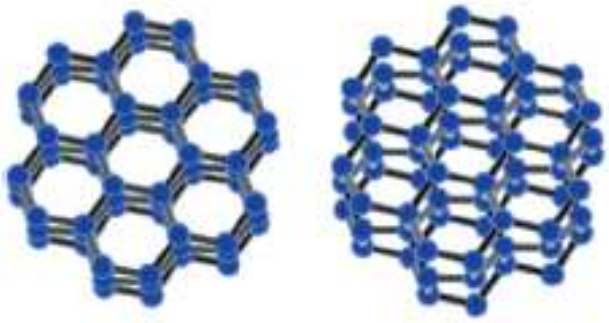

Figure 2.2: *Structure of ice crystals, showing the hexagonal lattice. The balls represent the oxygen atoms and the bars, the hydrogen atoms. From [Libbrecht, 2005].*

2.3 Crystal lattice anomalies

The perfect hexagonal crystal lattices rarely appear in nature. Most of the time, they show anomalies called defects. These defects are of two types, the *point defects* and the *dislocations* also called planar defects. The two next paragraph will give a brief description of these anomalies.

2.3.1 Point defects

By definition, an anomaly in the crystal lattice is a molecular composition that differs from the normal hexagonal lattice. Three main point dislocations must be distinguished, the *protonic point defects* the *vacancies* and the

interstitials.

The *protonic point defects*, also called *Bjerrum defects* proposed by Bjerrum

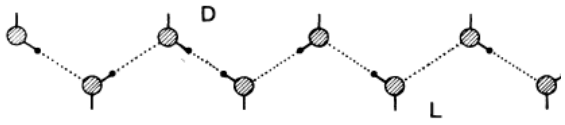

Figure 2.3: *Bjerrum defects in the ice crystal lattice. The "D" stands for the D-defect and represents a bond that is occupied by two protons. The "L" stands for the L-defect and represents an empty bond. From [Pnevmatikos, 1988].*

(1951) reflect a thermal equilibrium problem. Each molecule orientation is determined by its neighbours. Therefore, if a single molecule is turned to a

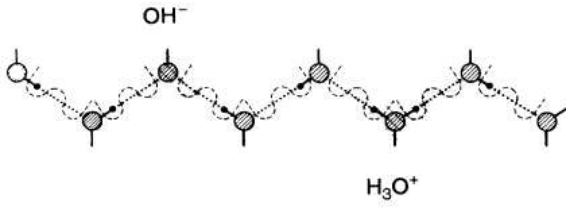

Figure 2.4: *Ionic defects in the ice crystal lattice. The protons can jump in a second equilibrium and generate a OH^- ion and a H_3O^+ one. This affects the distribution of charges but do not change the number of protons. From [Pnevmatikos, 1988].*

new orientation, it produces one bond with no protons and another in which two protons are pointing towards one another. The empty bond is called *L-defect* and the bond occupied by two protons is called *D-defect*, see figure 2.3. Another protonic related defect, shown in figure 2.4, the *ionic defect*

appears when a proton transfer occurs between two neighbouring molecules. Typically, the H_3O^+ and the OH^- are the protons that are moved, due to the ionization reaction

$$2H_2O \rightleftharpoons H_3O^+ + OH^-$$

Finally, two more *point defects*, the *interstitials* and the *vacancies*. The *vacancies*, as shown in figure 2.5, represent a *free space* in the crystal lattice, due to a missing molecule. On the other hand, the *interstitials*, as shown in figure 2.6, are represented by a free-crystal that appears in the *free space*, between the regular lattice layers. This occurs when the ice is cooled down to temperature at about -40°C.

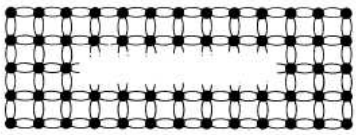

Figure 2.5: *Vacancies in the ice crystal lattice. The crystal lattice misses a molecule represented by the free space on the figure. Adapted from [Friedel, 1964].*

2.3.2 Dislocations

Dislocations are linear defects in the crystal lattice, where the regular atomic arrangement is disturbed [Kossevich, 1999]. Two models of dislocations are distinguished: the *edge* dislocations, as shown in figure 2.7, in which an additional half-plane is inserted into a part of the regular crystal lattice. The lattice structure is then distorted. In the other model (see figure 2.8), the *screw* dislocations, a part of a grain is inserted into the intermolecular space of an otherwise perfectly layered structure. Dislocations are commonly associated with deformation, even though the deformation usually occurs far from the dislocation [Kossevich, 1999]. Dislocations typically originate at the crystal boundaries, where local stress concentration can arise. Then, they move through the crystal lattice following two different processes; *glide* and *climb*.

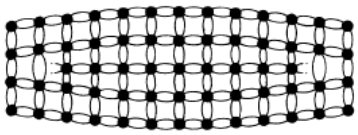

Figure 2.6: *Interstitials in the ice crystal lattice. The crystal lattice hosts a free-crystal between the regular lattice layers, which produces the deformed crystal lattice of the figure. Adapted from [Friedel, 1964].*

The slide motion of the dislocations appears when the slip plane is associated with plastic deformation of the crystal. The core of an edge dislocation in the crystal lattice (see figure 2.7) can also be displaced perpendicularly to the glide plane, either by addition or by removal of atoms from the end of the extra half-plane; this process is known as *climb*. Petrenko, V.F. and R.W. Whitworth (2002) added that climb movement requires molecular diffusion within the material, where glide does not.

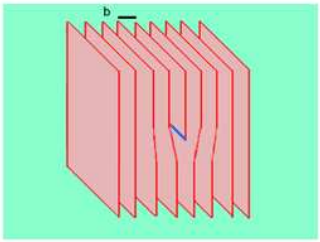

Figure 2.7: *Edge dislocation in a crystal lattice. An additional half-plane (represented by the plane with blue boundary) is inserted into the regular crystal lattice. From Wikipedia Encyclopedia.*

2.4 Deformation of a single ice crystal

Ice, like other crystalline solids deforms with both an elastic and a plastic component [Petrenko and Whitworth, 2002]. If a small amount of stress (force) is applied to ice for a short period of time, the ice will elastically deform (strain). Then, when the stress is removed, the ice will return to its initial shape. If the applied stress exceeds a certain amount, the ice will be deformed irreversibly; this is plastic deformation. According to Paterson (1994), single ice crystal normally deforms by gliding on its basal planes. If the applied stress is parallel to the basal plane, or with and angle that does not exceed 45° from the basal plane, the gliding is referred as an *easy gliding*. On the other way, if the stress is applied perpendicular to the basal plane, only little deformation occurs. This orientation is referred as *hard gliding*. Weertman and Weertman (1964) stated that the deformation of ice can simply be explained in terms of movement of dislocations (defined in the previous paragraph) within the crystals.

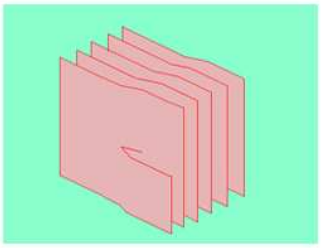

Figure 2.8: *Screw dislocation in a crystal lattice. A part of another grain (the gap on the left side of the molecule) is inserted into the intermolecular space of a molecule. From Wikipedia Encyclopedia.*

2.5 Deformation of polycrystalline ice

As evoked before, polycrystalline ice represents an aggregate of ice crystals, "in which the orientation of each single crystal is random and subjected to a constant stress" [Paterson, 1994]. The amount of stress, together with the time that it is applied on the aggregate result in different strains. Typically, the strain is plotted as a function of time to show the phases of deformation and/or creep. When a short-time stress is applied, the deformation is elastic.

Under further continuous stress, the strain is then divided into three stages, the *primary creep*, the *secondary creep* and the *tertiary creep*. These three deformations are plastic, which means that the ice will nether return to its initial state. As mentioned above, in the section 2.3.2, dislocations are closely related to deformation. Alley (1992) stated (from laboratory observations), that for densified ice, like in ice-sheets, deformation was primarily controlled by dislocation glide on the basal plane. But since each individual crystal in aggregates of polycrystals is confined by its neighbours, the glide on the basal plane must be accompanied by other processes such as rotation of the crystals relatively to each others, recrystallization and grain boundary sliding. In aggregates, individual crystals orientation is not always favorable to basal gliding in the direction of the applied stress. This results in the fact that polycrystalline ice deforms much more slowly than the single crystal ice.

2.6 Flow-law for ice

Stress, strain and strain rate are keywords to describe the flow-law. Numerous laboratory experiments have been accomplished to try to understand the flow relation for ice, as well as the parameters that control it. From these experimental works, the flow-law also called *Glen's law* has been established. It is generally expressed as

$$\dot{\varepsilon} = A\sigma^n \tag{2.1}$$

where $\dot{\varepsilon}$ is the strain rate, σ the stress deviator, n the power law constant and A a factor depending on the temperature according to the *Arrhenius relation*: $A = A_0 exp(-Q/RT)$. In which, Q is the activation energy for creep, R the universal gas constant and T the temperature. The value of A_0 depends, among other factors, on the ice fabric, the grain size and the impurity content. From the results of field and laboratory work, n is approximated to 3.

2.7 Recrystallization in ice from ice-sheets

Ice from polar ice-sheets is characterized by three recrystallization processes which have different terminologies defined by respectively Alley (1992) and Duval and Castelnau (1995). The definitions referred in this thesis are the ones described by Duval and Castelnau (1995).

The three terms, *grain growth*, *rotation recrystallization*, first introduced by Poirier (1985) and *migration recrystallization* reflect a division of the ice-sheet in three depth zones, where each of these recrystallization processes

occurs. It is though important to notice that each process is not restricted to one area. In other words, several processes can occur in the same zone.

2.7.1 Grain growth

Grain growth, also called *normal grain growth* occurs in the first few hundreds meters of most of the central parts of ice-sheets, both in firn and ice. Grain growth is driven by neighbouring grains that possess different energy levels due to the curvature of energetic grain boundaries and/or different amounts of accumulated strain energy. A pressure gradient induced by the curved boundaries of two grains leads to molecule movement, where they move from the higher-energy state (grains with concave form) to the lower-energy state (grains with convex form). Consequently, the average grain-size trends to increase, to reach a minimization of the surface energy [Alley, 1992]. Alley *et al.* (1986) remarked that this process would continue indefinitely in pure ice, but since ice from ice-sheets also contains microparticles, bubbles and dissolved particles, grain boundary migration is disturbed. The grain growth velocity, v can be obtained from the following equation

$$v = \mu \frac{\gamma}{R} \tag{2.2}$$

where μ is the mobility, γ the grain boundary free energy and R the grain radius. In the equation 2.2, the ratio γ/R represents the driving force. Like Alley *et al.* (1986), Weiss *et al.* (2002) distinguished two different types of impurities effects on grain growth: the drag of the soluble impurities (the ones which are dissolved as ions when ice is melted) by grain boundaries and the *pinning* of the grain boundaries by the insoluble impurities (dust). In the first case, the impurities are dragged by the moving boundaries, which results in a lower mobility μ, and consequently in a reduction of the velocity of the grain growth. But since it only slows the process down, it will affect all the grains equally and the normal distribution of grain size should remain unchanged. In the second case, the impurities are not dragged by a reduction of the mobility, but by a modification of the driving force for boundary migration (γ/R), which inhibits the grain growth process. Consequently, the pinning of the impurities modifies the normalized distribution of the crystal size [Riege et al., 1998].
To predict the average area of grains, the parabolic growth relation has been defined as it follows

$$R^2 - R_0^2 = 2Kt \tag{2.3}$$

where R_0 represents the initial grain size, K the *Arrhenius* temperature dependent constant and t, the time.

2.7.2 Rotation recrystallization

The rotation recrystallization, also called *polygonization* is a process that is essentially dependent on temperature and grain size. Rotation recrystallization is a process of formation of new grains by subdividing the old grains [Alley, 1992]. This process usually takes place when the grain, or different parts of the grain are subjected to different stress states, in that case, the grain becomes bent or twisted. The lattice of a deforming crystal rotates and acquires a curvature, leading to an increase in the dislocation density, and thus in the elastic strain energy.

2.7.3 Migration recrystallization

The migration recrystallization, also called *recrystallization* is a process that leads to the nucleation of new grains, associated with a rapid migration of the grain boundaries. Kamb (1972) noticed that the new grains in migration recrystallization usually form in energetically favored orientations with their c-axes at high angles ($\approx 45°$)to compressional axes. Migration recrystallization usually occurs at temperatures above $-15°C$ [Weiss et al., 2002].

2.8 Optical properties of ice: the influence of the C-axis

Double refraction of ice

Since ice is of the hexagonal form, the crystals are *anisotropic*. Therefore, when a light beam enters the crystal, it breaks into two waves that travel with different velocities through the crystal. Such a property is called *double refraction* or *birefringence* [Hobbs, 1974]. One of the waves, the *ordinary wave* travels with the same velocity through the whole crystal, while the other one, the *extraordinary wave* travels with different velocities, depending on the direction of propagation of the beam. In a very special case, hexagonal crystals can also behave isotropically[1] if the entering light beam is travelling along the c-axis of the crystal (see figure 2.1); in that case, the last axis is also defined as the *optic axis* of the crystal.

[1]The velocity of propagation is the same in all directions

Analysis of ice with polarized light

When a light beam enters a cross-polarizer, and if the polaroids screens are orthogonal to each others, the whole light will be absorbed, as shown on the figure 2.9. Consequently, if a crystal is placed between crossed polaroids, with

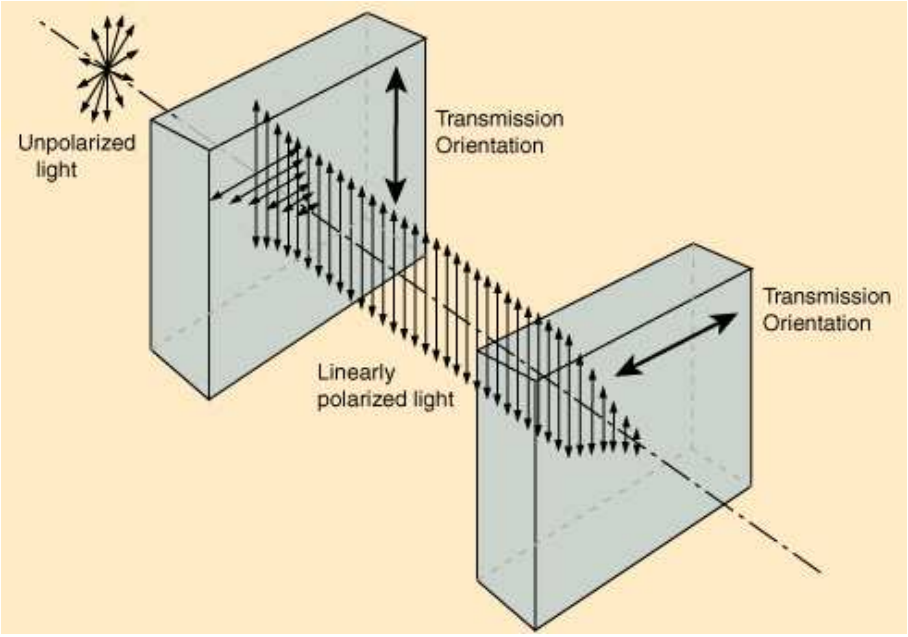

Figure 2.9: *The cross-polarization of an unpolarized light beam (circular spectrum). When passing through the first polaroid, the unpolarized light is "filtered" and leaves with only one the horizontal component of the original spectrum. Then it comes to the second polaroid, which only lets the horizontal component pass through; therefore, the light is completely absorbed.* (Taken from www.hyperphysics.phy-astr.gsu.edu/hbase/phyopt/polcross).

its c-axis in the direction of the beam of light, the following happens: the light emerging from the first polaroid screen will be transmitted unchanged, but due to the perpendicular orientation of the second polaroid screen, the crystal appears dark. If the crystals are differently orientated, some light will pass the first polaroid screen and then will be transmitted to the second polaroid screen. This is though for one single crystal, so if the same beam is sent through polycrystalline ice, the difference of orientation of each single grain of the aggregate would result in a different transmitted colour. In that way, it is possible to determine the exact orientation of the c-axis of each grain of the aggregate. To accomplish this operation, Langway (1958) proposed to use a *universal stage* (also called the *Rigsby Stage*, further described in the next chapter). When unpolarized (white) light is sent through a crystal, it

may appear coloured between the cross-polarizer, due to an interference of wavelengths. Therefore, it is important to insure that the analyzed sample is of the right thickness. Basically, when a beam of visible light (violet) is sent through a crystal that is just too thick, the two waves are emerging just out of phase. Consequently, the obtained yellow-green colour represents the substraction of the violet light from the white light. Increasing thickness would respectively remove: the blue wavelength to let the orange appear, the green for the red, the yellow for the violet, the orange for the blue and the orange for the green. These interferences in colours have been defined as the *first-order interference colours* by Hobbs (1974). In the same way, the *second-order interference colours* are defined when the emerging waves are out of phase with exactly 2 wavelengths, and the *third-order interference colours* when the emerging waves are out of phase with exactly 3 wavelengths.

Chapter 3

Measurements on the NGRIP ice core

The coming chapter will essentially deal with their analysis that enabled the sample preparation together with the performed measurements. To begin with, I will resume the processes that the ice core went through, from the drilling on the site to its storage at the university, where it is ready to study. Hereafter, I will present my samples and give some explanations about the choice of these, and which processes they got through before they are ready to analyze.

3.1 From core extraction to storage

The NGRIP camp has a science trench where the ice core is transported right after its extraction. In this science trench, where the temperature rarely exceeds $-15°C$ to avoid a post-drilling recrystallization [Gow, 1994], the core is logged, its conductivity recorded by Electrical Conductivity Measurement (ECM) and its stratigraphy reproduced by a line scan. Then, the core is divided into five pieces along its length, the main core, that consists of half of the cylindrical core and four smaller parts, used for the ice physical properties, the gas analysis, chemical and dust content analysis (CFA), the isotropic composition. For logistic convenience, the kept main core is then cut and numbered into sections of 0.55 m, stored into plastic bags and shipped to Copenhagen, where it is stored in a freezer.

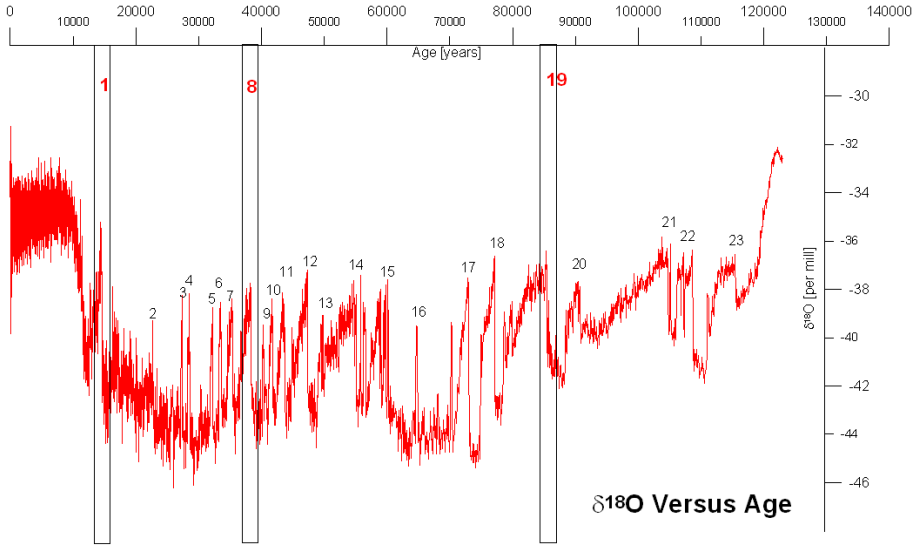

Figure 3.1: $\delta^{18}O$ *versus Age.*

3.2 Choice of the samples

The six selected samples, numbered on the table 3.1, are covering three Dansgaard-Oeschger (D.O.) events (see paragraph 1.2.1), the D.O. 1 (Bølling), the D.O. 8 and the D.O. 19, as shown on the figure 3.1. For each of these events, six thin sections have been made, three from the warm period and three from the cold one. The transition period is avoided, since one of the purposes of this study is to analyze the influence of rapid climatic changes on the crystals properties. The next step was to be aware of the small climatic variations either within the warm or the cold part of the selected samples. Therefore, a detailed plot of the exact position of the analyzed sections is presented for each of the events. Figure 3.2 does not reveal any special or abnormal spike in the chemical components that could be considered as a determining or influencing factor on ice crystals analysis. The same can be observed on figures 3.3 and 3.4 that respectively represent the D.O. 8 and 19, even though insignificant small variations in the calcium and sodium concentrations can be seen. The samples are vertical samples, which means that the thin sections have been cut along the core, as shown on the figure 3.5, to enable a continuous analysis of the climate evolution. Due to technical/practical problems under the preparation of the sections, like total or partial breaking of the thin ice section, some samples cannot provide a continuous data set. An accident occurred with the thin section NG3770C,

Event	*Bag/Sample Number*	*Depth at the top of the section [m]*
D.O. 1 (Warm)	NG2915A	1602,70
D.O. 1 (Warm)	NG2915B	1602,80
D.O. 1 (Warm)	NG2915C	1602,90
D.O. 1 (Cold)	NG2924A	1607,65
D.O. 1 (Cold)	NG2924B	1607,75
D.O. 1 (Cold)	NG2924C	1607,85
D.O. 8 (Warm)	NG3758A	2066,35
D.O. 8 (Warm)	NG3758B	2066,45
D.O. 8 (Warm)	NG3758C	2066,55
D.O. 8 (Cold)	NG3770A	2072,95
D.O. 8 (Cold)	NG3770B	2073,05
D.O. 8 (Cold)	NG3770D	2073,25
D.O. 19 (Warm)	NG4605A	2532,75
D.O. 19 (Warm)	NG4605B	2532,85
D.O. 19 (Warm)	NG4605C	2532,95
D.O. 19 (Cold)	NG4615A	2537,70
D.O. 19 (Cold)	NG4615B	2537,80
D.O. 19 (Cold)	NG4615C	2537,90

Table 3.1: *Table presenting the chosen samples with their bag number and their respective depth.*

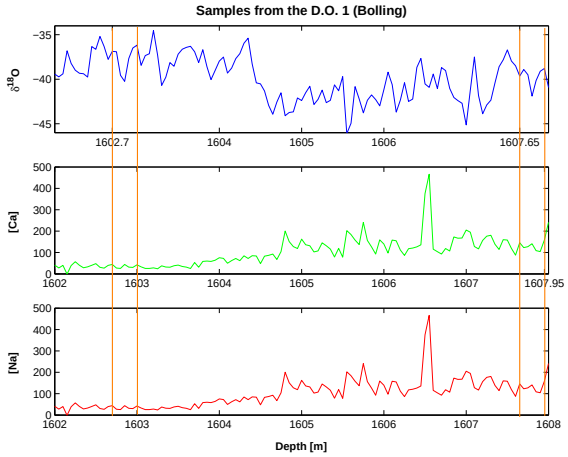

Figure 3.2: *Thin section detailed position of the D.O. 1 expressed in* $\delta^{18}O$, $[Ca^{2+}]$ *and* $[Na^{+}]$.

which has been replaced by the NG3770D.

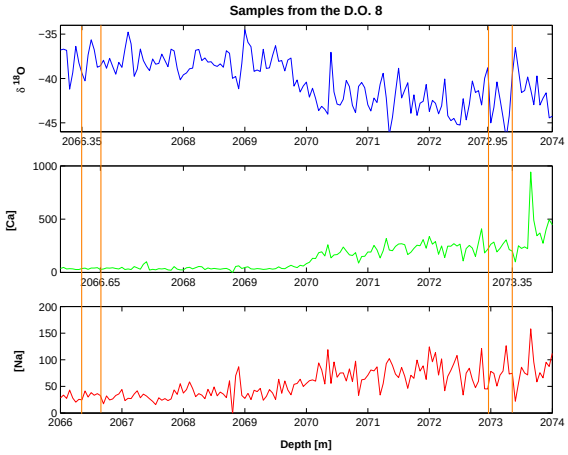

Figure 3.3: *Thin section detailed position of the D.O. 8 expressed in* $\delta^{18}O$, $[Ca^{2+}]$ *and* $[Na^{+}]$.

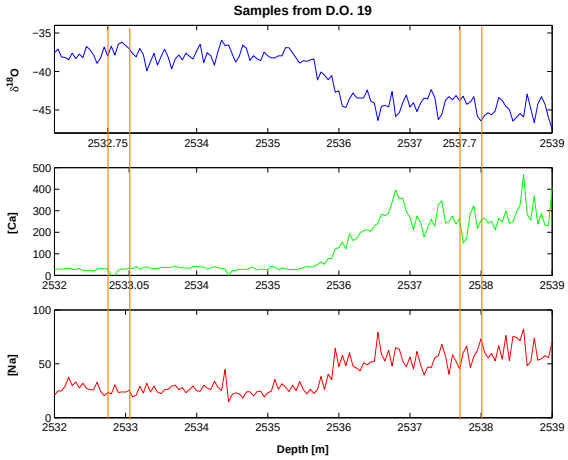

Figure 3.4: *Thin section detailed position of the D.O. 19 expressed in* $\delta^{18}O$, $[Ca^{2+}]$ *and* $[Na^{+}]$.

3.3 Sample preparation

Once the right bags containing the main core pieces were found in the main freezer, a 1 cm thick section was cut with a bandsaw along the 55 cm core for each of the 6 bags. Each of these sections have then been further divided

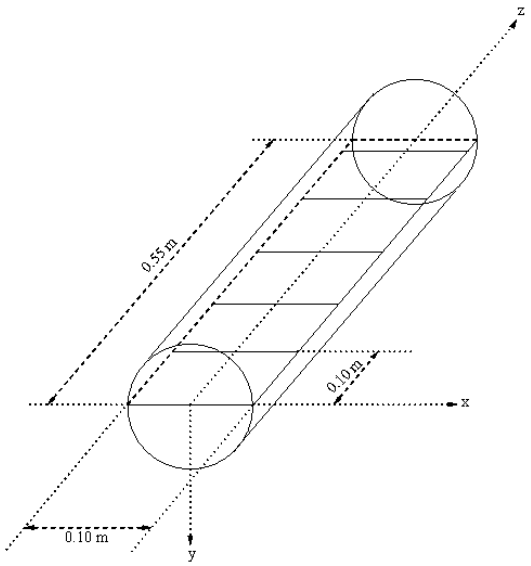

Figure 3.5: *Thin section extraction along the main ice core.*

into 5 sections of 10 cm in order to obtain 5 pieces of 10 x 10 cm samples (see figure 3.5). The last 5 cm are not used in this project. The next step in the preparation of the thin sections is to reduce the 1 cm thick section to about 0.3 mm thickness, by using a microtome, such as shown on the figure 3.6. The process is performed in the cold laboratory, where the temperature is of about $-15°C$. The accomplishment of this procedure starts with a flattening of the sample, by mounting the 1 cm thick section on a glass plate with the help of droplets. Once the flat surface is obtained, the sample is turned and carefully mounted with the flat surface on an other glass plate and fixed all the way around with water droplets. It is important that no air is trapped between the glass plate and the sample. Then, the thinning of the sample can start. The bag number and an arrow showing the orientation of the sample are written on the glass plate, in order to handle it properly in the analysis. The sample is finally stored in a plastic bag to ensure that it is protected against the eventual surrounding contamination, sublimation and recrystallization. The room temperature of $-15°C$ should prevent the post-drilling recrystallization since Duval and Castelnau (1995) remarked that the migration recrystallization only takes place at temperatures higher than about $-10°C$.

The overall quality of the thin sections is quite good, even though some of them present some cracks. In fact, the cracks complicate the crystal analysis. They can be interpreted as crystal boundaries, and spoil the data. Their thickness, which is an important parameter for the following analysis, ap-

Figure 3.6: *Thin section thinning by using the microtome bench.*

pears to be even. The thickness can be rapidly checked by putting the thin section in a cross polarizer. When the section has the wished thickness and is even thick, the colour, in a brownish tone, is the same through the whole section. A colour gradient would reveal an unequal thickness. A thickness comparison between two thin sections is presented on the figure 3.7. The purpose of getting samples in the brownish scale is to ensure the quality of the *c*-axis measurements and to enable an acceptable determination of the grain boundaries, which is the next step in the process.

Figure 3.7: *Comparison between two thin sections: left, a thin section (4605C) showing a color gradient, reflecting an uneven thickness. Right, a thin section (2924C) showing an even color scale reflecting an even thickness.*

3.4 Data acquisition

The 18 thin sections have been measured at the Ice and Climate Group, Niels Bohr Institute, University of Copenhagen, on a new automatic *c*-axis analyzer (see figure 3.8), developed in Australia by D.S. Russell-Head. The analyzer measures the fabric of individual crystals by using image-processing techniques. The main components of the analyzer consist on a *sample stage*, a pair of *rotating crossing polaroids*, a *CCD camera* and a *light source*. Basically, each individual grain is brought to extinction, to obtain information about the orientation of the *c*-axis. It is almost the same process used in the Rigsby Stage[1], but with better statistics than possibly with manual measurements, because all the grains in the thin section are measured. Svensson *et al.,* (2003) gave a description of the functioning of the analyzer, and how the data are sampled. I recommend this article for further details.

Once the thin sections are digitalized by the automatic *c*-axis analyzer

Figure 3.8: *Automatic c-axis analyzer.*

to produce pictures such as shown on figure 3.9, the data are then further processed through two softwares packages, *Image Pro* and *Virtual Basic*, in order to draw the outlines of each individual crystal on each thin section. *Image Pro* produces the first suggestion of outlines. But even though the samples are plane, some manual corrections must be performed. The borders of the thin sections have to be redefined and each single crystal boundary must be checked, accepted or corrected. The final outline looks like the one

[1]A description of the Rigsby Stage will be done in the section 4.2: Fabric parameters measurements.

shown in figure 3.10. The obtained outlines are then processed again using the *Texture Toolbox* to get the final texture that provides the raw data. These raw data are the crystal area, A_k, the collateral and azimuthal angles θ_k and φ_k of the c-axis orientation for each grain k. From these 3 parameters, the microstructural (mean grain size and shape of the grain) and fabric (degree of orientation and second-order tensor) parameters (see chapter 4) can be computed by using the *Texture Toolbox*.

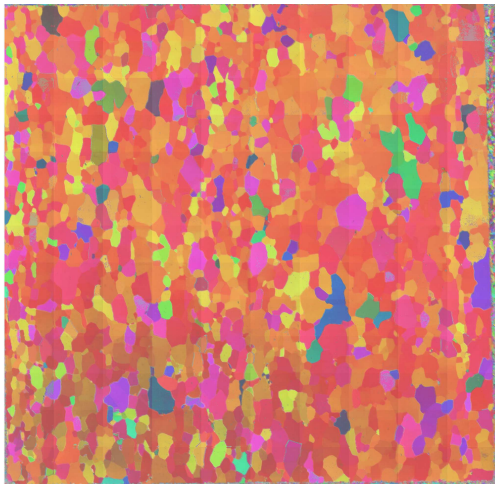

Figure 3.9: *Picture of the thin section 3758B extracted from the c-axis analyzer.*

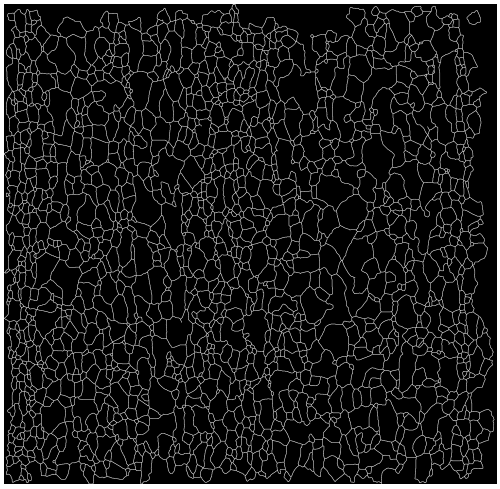

Figure 3.10: *Final picture of the produced outline for the thin section 3758B.*

3.4.1 The sectioning effect

A thin section is only a two-dimensional representation of the crystals, hence, it only gives limited information concerning the three-dimensional image of the grains shapes. In other words, two-dimensional thin section has its limitations. The appearing grains are not necessary visible at their maximum size, which means that the measured grain diameters will generally be lower than they truly are. This is called the *sectioning effect*. This effect has a major consequence in the determination of the size of the grains; a two-dimensional cut does inform about the grains size. Different authors have tried to compensate this loss by applying some correction factors, or by only counting chosen grains considering the size or other parameters. Since the main purpose of this thesis is to compare the relative variation of the grain size between different climatic periods of recrystallization, the real size of the grains is not of the biggest importance. A problem could arise when the results from this project are compared to the ones of other works, such as Thorsteinsson (1996) or Wang *et al.* (2002). But since the method they respectively used to compute their crystal area is either the *linear intercept method* [2] or the same as in this project, the same sectioning effect acts, and can therefore be ignored.

[2] See section 4.1.1

Chapter 4

Microstructure and fabric measurements on ice crystals: a theoretical approach

This section will give an approach to the theory behind the different measurements that can be made on ice crystals and how they can be interpreted. A presentation of the work done by Thorsteinsson *et al.,* (1997) on the GRIP ice core will illustrate the microstructural and fabric parameters when possible.
An introduction to the quantitative microstructural parameters will open this section, followed by some definitions of the fabric parameters; this to enable a general description of the texture of the thin sections.
In this work, *Microstructure* describes the grains size and shape, *fabric* covers all that is related to the orientation of the grains and finally, *texture* covers both microstructure and fabric. This distinction was first introduced by Lliboutry (1965) .

4.1 Microstructural parameters measurements

Due to different interferences in colours, individual grains and grain boundaries can be shown by placing a thin section between cross polarizers. The changes in colour reflect different orientations of the c-axis of the different grains, as it has been previously described (see Section 2.8).

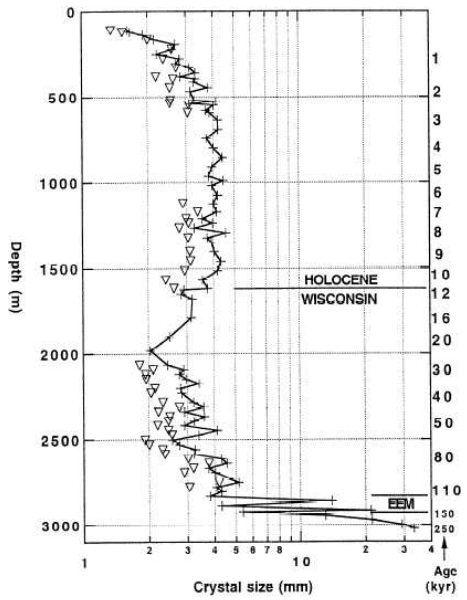

Figure 4.1: *GRIP crystal size (diameters) evolution with depth. The processes of normal grain growth, saturation and rotation recrystallization are respectivelly represented on the intervals, 0-1000 m, 1000-1600 m and 1600-2800 m. Taken from Thorsteinsson et al. (1997).*

4.1.1 Mean grain size

Usually, grain size is expressed either in mean area $< A >$ or in mean radius $< R >$. In figure (4.1), Thorsteinsson *et al.* (1997) show the grain size evolution by means of mean grain size diameter, which have been obtained with the *linear intercept method*. This method has originally been introduced by Gow (1969) and is based on the counting of the grain boundaries that a vertical (L_v) or horizontal (L_h) line intercepts. In more recent studies such as the one of Wang *et al.* (2002) and this thesis, the crystals areas are computed by counting the number of crystals (N_g) within a defined surface, as suggested by Duval and Lorius (1980) . In this thesis, the area (A) of the thin section is known (0.1 m $\times$ 0.1 m). The problem is that some grains have been rejected from the borders, but since the precise area of each grain (A_k) is known, the relation simply becomes: $A_k = A/N_g$. From that equation, the relation between the two methods can be established: $L = 1.5\sqrt{A}$ [Thorsteinsson et al., 1997], where L is either L_h or L_v. In this work, the mean radius $< R >$ will be the reference measurement to describe the grain

size. Durand *et al.* (2005) express the mean radius by the following relation:

$$\langle R \rangle = \frac{1}{N_g} \sum_{k=1}^{N_g} A_k^{1/2} \tag{4.1}$$

where $A_k = N_p^k \times \delta$ is the cross sectional area of the grain k, δ the area of one pixel and N_p^k is the number of pixels that compose the grain k.

Back now to figure 4.1, it appears clearly that the climatic changes have an impact on the crystal size. The graph can be divided in three main phases: the first one, from the surface to a depth of about 1000 m, which is characterized by an increasing in grain size (from ≈1.5 to 3.5 - 4 mm), resulting from the normal grain growth process due to the low impurities content. The second part covers the depth between 1000 and 1600 m, where the grain size stays constant (≈4 mm). This phase is probably the result of a saturation of the crystal size. The grains cannot grow anymore. This leads to the last part of the curve, from 1600 to 2800 m [1], where the grains got smaller again (≈2 mm), resulting from the rotation recrystallization process (see section 2.7.2). This process occurs because the grains are subjected to the stresses that the increasing dust concentration provokes. Towards the bottom, the grain are growing again, probably as a result of a combination between decreasing dust content and increasing temperature.

4.1.2 Grain size and impurities

Some previous works have been done to try to correlate impurities content and ice crystal size, *e.g.* Svensson *et al.* (2003)'s work on the Holocene ice from NGRIP. The next figure (figure 4.2) represents a correlation plot between the mean crystal area and the calcium concentration. This figure strongly influences the coming section of this thesis, where impurities and grain size will be analyzed, in order to try to get more information about this correlation.

4.1.3 The shape of the grains

The *grain shape* permits to quantify the anisotropy of the microstructure. Once again, among the different proposed theories, I will keep the one proposed by Durand *et al.* (2004) based on the vector $\vec{\ell}$ that defines the links

[1] The transition at 1600 m is called the Wisconsin-Holocene

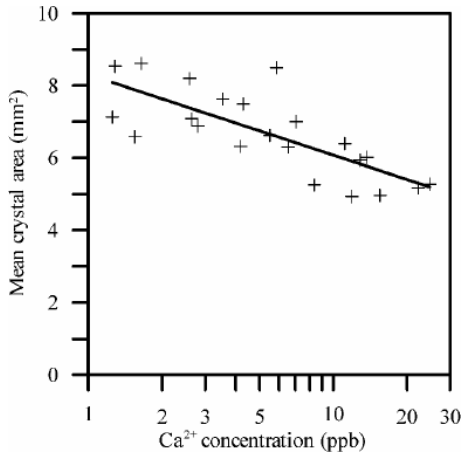

Figure 4.2: *Crystal area (from NGRIP) plotted as a function of the log of the calcium concentration. The correlation between these two parameters is a part of the background research of this thesis. (taken from Svensson et al. (2003)).*

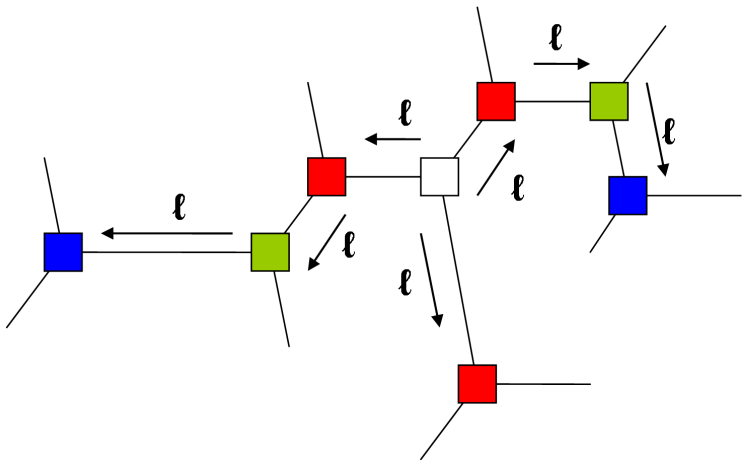

Figure 4.3: *Schematic representation of the vectors $\vec{\ell}$; the white cube represents the reference triple junction, while the reds, the greens and the blues respectively represent the first-, the second- and the third-order of triple junctions.*

between neighbouring triple junctions (see figure 4.3). A triple junction describes the place where three grain boundaries meet. The equation permitting to calculate the local average microstructure tensor $\overline{\overline{M}}$ is the following:

$$\overline{\overline{M}} = \left\langle \begin{pmatrix} \ell_x^2 & \ell_x\ell_z \\ \ell_z\ell_x & \ell_z^2 \end{pmatrix} \right\rangle_p = \frac{1}{N}\sum_{k=1}^{N} \vec{\ell}(k) \otimes \vec{\ell}(k) = \mathcal{R} \begin{pmatrix} \lambda_1 & 0 \\ 0 & \lambda_2 \end{pmatrix} \mathcal{R}^{-1}. \quad (4.2)$$

where $\mathcal{R}$ represents the rotation which diagonalizes the tensor $\overline{\overline{M}}$, λ_1 and λ_2 the corresponding eigenvalues, N the number of triple junctions quantified the rank of the chosen order of triple junctions, p (usually p=3). The eigenvalues are of great importance as λ_1, represented by its eigenvector e_1, determines the direction in which the crystals are the longest. In that way, they inform about the deformation of the grains.
The statistical strain tensor $\overline{\overline{U}}$ is the next important parameter that must be introduced. It is calculated by using the equation 4.3 shown below. $\overline{\overline{U}}$ represents the variation of $\overline{\overline{M}}$ from an original reference frame defined by the isotropic ice, $\overline{\overline{M_0}}$. The advantage in computing this parameter compared to $\overline{\overline{M}}$ is that it removes the information about the size that the parameter $\overline{\overline{M}}$ gives through the vectors $\vec{\ell}$.

$$\overline{\overline{U}} = \frac{1}{2}\mathcal{R} \begin{pmatrix} \log(\frac{\lambda_1}{\sqrt{\lambda_1\lambda_2}}) & 0 \\ 0 & \log(\frac{\lambda_2}{\sqrt{\lambda_1\lambda_2}}) \end{pmatrix} \mathcal{R}^{-1} = \frac{1}{4}\mathcal{R} \begin{pmatrix} \log(\frac{\lambda_1}{\lambda_2}) & 0 \\ 0 & \log(\frac{\lambda_2}{\lambda_1}) \end{pmatrix} \mathcal{R}^{-1}. \quad (4.3)$$

In this thesis, the reference two-dimensional frame for the vertical thin

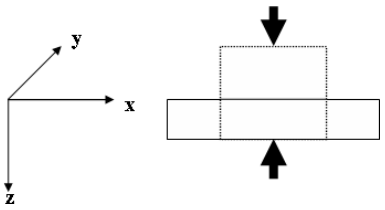

Figure 4.4: *Illustration of the uniaxial vertical compression (pure shear [Paterson, 1994]) along the z-axis. The dashed cube represents the original form and the elongated rectangle the new formed cube after submission to vertical compression represented by the thick black arrows.*

sections is defined by the x-z plane, where z represents the depth. The strain tensor has the following components: U_{xx}, U_{xz}, U_{zx} and U_{zz}, but since $U_{xx} = -U_{zz}$ and $U_{xz} = U_{zx}$, only two components are of relevant interest, in this case, U_{zz}, which represents the vertical compression, and U_{xz}, the

horizontal shear. Two small drawings can easily show how these tensor components react to the vertical compression and to the horizontal shear. On figure 4.4, the tensor components become: $U_{zz} = \alpha$ and $U_{xz} = 0$. And, on figure 4.5, the tensor components become: $U_{zz} = 0$ and $U_{xz} = \alpha$. α stands for a number, which defines the magnitude of the tensor component.

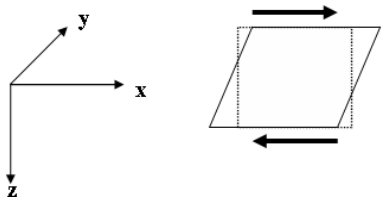

Figure 4.5: *Illustration of the horizontal shear (simple shear [Paterson, 1994]) along the x-axis. The dashed cube represents the original form and the sheared one, the new formed cube after submission to horizontal shear represented by the black arrows.*

4.2 Fabric parameters measurements

The fabric of a thin section containing N_g crystals can be described by different parameters that represent the distribution of the *c*-axes. Among them, the conventional reference parameter, the degree of orientation R and the newer one, the second-order tensor $\mathbf{a}^{(2)}$. The coming paragraph will introduce these parameters and the methods that enable their determination.

4.2.1 The Rigsby stage

The *Rigsby stage*, also called the *universal stage* is a material that enables the distinction and the orientation of individual grains. A thin section is placed on a mount, that can be rotated both vertically and horizontally, between the crossed polaroids. Because each grain transmits a different amount of light according to its orientation, the orientation of the grain can be found by a simple manipulation. This latest consists on rotating the mount until the chosen grain appears dark; in that case, as explained above, its *c*-axis is parallel to the direction of the transmitted light, and its degree of inclination can be noted.
This laborious manual process has been later ameliorated and replaced by semi-automatical and then automatical instruments, on the basis of the same measurement method. In this project, I use the Automatic *c*-axis analyzer

and some imaging processing tools, that provide the c-axis orientations automatically. Further information concerning the details of the calculations that enabled the determination of the degrees of orientation of the concerned samples will be presented in the next paragraphs.

4.2.2 C-axis measurement: the orientation $\mathbf{c}^k$

The orientation ($\mathbf{c}^k$) of each grain or crystal k can be determined by defining the two angles that allow to get the direction of its c-axis. The first angle is the *colatitude* θ_k, which represents the tilt of the grain's main axis and the second one is the *longitude* or *azimuth* φ_k. These two angles must be measured in an agreed reference frame. In this project, the reference coordinate system is set to be with the vertical thin section on the x-z plane and the unit vector $\mathbf{y}$ pointing orthogonally to the thin section, as shown on figure 4.6. The expression of $\mathbf{c}^k$ in cartesian coordinates becomes:

$$\mathbf{c}^k = (\cos\varphi_k \sin\theta_k, \sin\varphi_k \sin\theta_k, \cos\theta_k) \tag{4.4}$$

4.2.3 The volume weighted fraction f_k

Gagliardini *et al.* (2004) proposed to analyze the volume weighted fraction, f_k for each grain k. The volume weighted fraction consists on estimating the volume of the grain k as a function of its cross section areal fraction A_k measured on the thin section. Consequently, the following equation is obtained:

$$f_k = \frac{A_k^{3/2}}{\sum_{j=1}^{N_g} A_j^{3/2}} \tag{4.5}$$

where N_g represents the number of grains of the sample.

4.2.4 The degree of orientation R

The *degree of orientation* R, also called the *strength of fabric* has been previously described by different authors such as Thorsteinsson (1996), Thorsteinsson *et al.* (1997) and Castelnau *et al.* (1998). To determine this parameter, it is necessary to assume that each c-axis for each grain ($\mathbf{c}^k$) is represented by a vector within the agreed reference hemisphere as shown in figure 4.6. A problem occurs with this method when the c-axis are pointing in the opposite direction of $\mathbf{z}$. In that case, they would vanish when summed. The equation,

$$R = 2||\sum_{k=1}^{Ng} f_k \,\mathrm{sign}(\bar{\mathbf{c}}.\mathbf{c}^k)\mathbf{c}^k|| - 1 \tag{4.6}$$

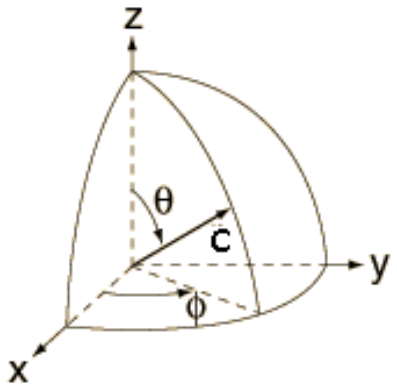

Figure 4.6: *The c-axis of a grain k in the reference unit hemisphere.*

where ‖.‖ represents the norm of a vector, must include a special function to correct the eventually negative sign of the vector $\mathbf{c}^k$ as mentioned above. It is the case with the "sign-operator" function, which takes into account the fact that the vector sum should be calculated by taking $+\mathbf{c}^k$ when $\mathbf{c}^k$ belong into the reference half hemisphere centered on $\bar{\mathbf{c}}$ and $-\mathbf{c}^k$ when $\mathbf{c}^k$ points out of this half hemisphere [Durand et al., 2005]. $\bar{\mathbf{c}}$ on equation 4.6 stands for the best fabric symmetry axis representing the orientations ($\mathbf{c}^k$) of all the grains of the sample. To better understand how $\bar{\mathbf{c}}$ is obtained, the introduction of the of the equation 4.7, that enables the calculation of the useful eigenvalues is necessary.

When the *c*-axis are randomly oriented, the degree of orientation R equals zero, oppositely, when they are all pointing in the same direction, R equals 1. It is important to notice that two thin sections can have an almost equal R, but a different fabric e.g. a girdle-like fabric can have similar R to a single maximum fabric, because of the ratio between the eigenvalues (more details about of the fabric types and the eigenvalues developed in the section 5.2). The figure 4.7 illustrates the degree of orientation plotted as a function of depth for the GRIP ice core that Thorsteinsson *et al.* published in 1997. On that figure, it is seen that R increases with depth, in the interval 500-2800 m, which signifies that the grains are more oriented with depth, or that the fabric gets stronger with depth. At the top and at the bottom of the ice core, R seems to be randomly oriented with a weaker fabric. R is though an historical parameter that has been used to describe fabrics since ice crystal studies began. In this thesis, the second-order tensor $\mathbf{a}^{(2)}$, which has the

advantage to inform about the orientation distribution, will be user.

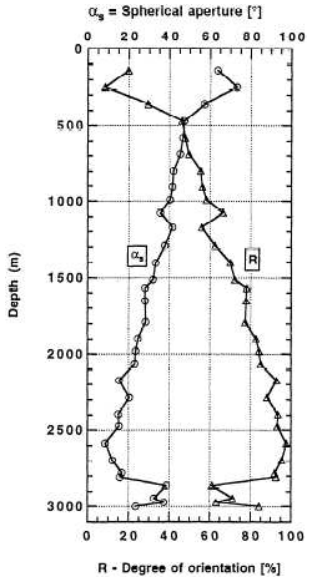

Figure 4.7: *GRIP spherical aperture (α_s) and degree of orientation (R) as a function of depth, taken from Thorsteinsson et al. (1997).*

4.2.5 The second-order tensor $\mathbf{a}^{(2)}$

The eigenvalues for the grains are obtained from the second-order tensor[2], $\mathbf{a}^{(2)}$ written below:

$$\mathbf{a}^{(2)} = \sum_{k=1}^{N_g} f_k \mathbf{c}^k \otimes \mathbf{c}^k \tag{4.7}$$

The eigenvalues are noted $\mathbf{a}_1^{(2)}$, $\mathbf{a}_2^{(2)}$, $\mathbf{a}_3^{(2)}$ and their corresponding eigenvectors $\mathbf{e}_1$, $\mathbf{e}_2$, $\mathbf{e}_3$. $\bar{\mathbf{c}}$ corresponds to the largest eigenvalue, $\mathbf{a}_1^{(2)}$, while its direction is defined by the corresponding eigenvector $\mathbf{e}_1$. The eigenvalues represent the length of the axes of the ellipsoid that fit the best the density distribution of the grain orientations, as suggested by Woodcock (1977) . The eigenvectors define the axes direction of this ellipsoid. Some important relations exists between these eigenvalues, notably that $a_1^{(2)} > a_2^{(2)} > a_3^{(2)}$, that the sum of the three values must equal 1 ($a_1^{(2)} + a_2^{(2)} + a_3^{(2)} = 1$), but also that the fabric of the sample is of the girdle type when $a_1^{(2)} \approx a_2^{(2)} > a_3^{(2)}$, and of the single

[2]Further details concerning these tensor operations are presented in the article written by Durand *et al.* (2005).

maximum type when $a_1^{(2)} > a_2^{(2)} \approx a_3^{(2)}$.
From this eigenvalues, Woodcock (1977) computed the so called woodcock parameter, k, which distinguishes the two previously named types of fabric, the girdle and the single maximum. k is calculated as it follows:

$$k = \frac{ln(a_1^{(2)}/a_2^{(2)})}{ln(a_2^{(2)}/a_3^{(2)})} \tag{4.8}$$

When k<1, the fabric is of the girdle type and when $k > 1$, it is of the single maximum type.

4.2.6 The spherical aperture α_s

The *spherical aperture* α_s represents half the apex angle of a cone that contains 90% of the measured c-axis. α_s is defined as below,

$$\alpha_s = \arcsin\sqrt{1-R} \tag{4.9}$$

Figure 4.7 also illustrates the spherical aperture plotted as a function of depth for the GRIP ice core that Thorsteinsson *et al.,* published in 1997. The smaller the α_s (from 0° to 90°), the stronger the fabric. For that reason, this parameter is commonly related to the strength of fabric. But since the spherical aperture is generally associated to the degree of orientation, R, this thesis will neither calculate nor present the spherical aperture parameter.

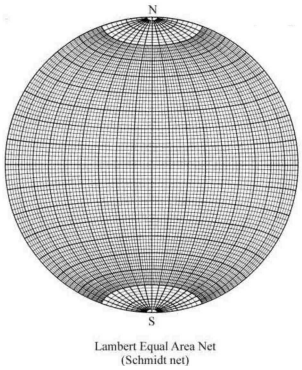

Figure 4.8: *The Schmidt equal-area net.*

4.2.7 Graphical representation of $\mathbf{c}^k$: the Schmidt diagram

The Schmidt diagram is constructed on the Lambert-projection and represented on the Schmidt equal-area net, see figure 4.8. The projection of $\mathbf{e}_1$,

obtained (from equation 4.7) is plotted on the Schmidt diagram with a red cross, as shown on the figure 4.9. All the other dots on the diagram are representing the projections of the intersections of the c-axis ($\mathbf{c}^k$) of all single grains with the surface of the reference half hemisphere.

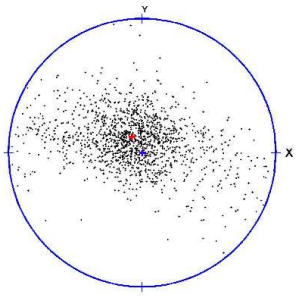

Figure 4.9: *An example of a top view Schmidt diagram taken from my own data (NG2915B - D.O. 1 - Bølling).*

4.3 GRIP versus NGRIP

Two previous analysis of the texture (microstructure and fabric) on the GRIP ice core have been carried out by Thorsteinsson (1996) and Hansen (2001) . They both released interesting and consistent data on their respective publications. The next step was then to enable a comparison with the obtained results from the newer ice core drilled at NGRIP. Like Svensson (2003) did on his experiment on the NGRIP late-to middle-Holocene ice, a correction factor, estimated to 1.5 will be used in this thesis to enable the comparison of the crystal area of the NGRIP results with the ones of GRIP. The GRIP data that are used in this paper have been provided by Thorsteinsson[3] from which the L_h values (the only continuous ones) are used to establish the comparison between the size parameters of the two different data sets. The comparison plot between the GRIP data and the NGRIP ones (provided by Wang *et al.* (2002)) is shown on figure 4.10. Due to the fact that the two data sets come from two different drilling sites, it is not possible to compare their continuous evolution with depth. The evolution of the crystal area is an information about climate; therefore, two events of the same depth have a different age at GRIP and at NGRIP. For this reason, the graph presents two

[3]The GRIP data can be downloaded from the following link provided by Thorsteinsson: http://www.ncdc.noaa.gov/paleo/icecore/greenland/summit/.

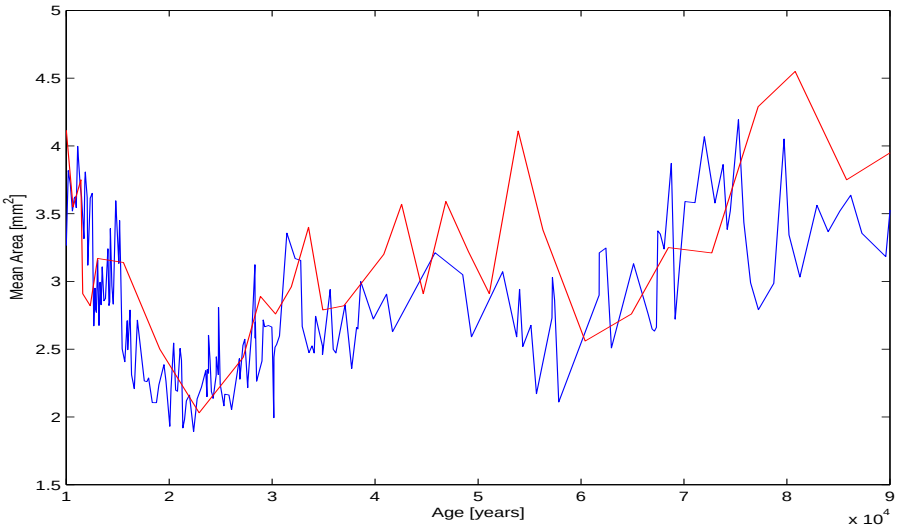

Figure 4.10: *Comparison of the evolution of the mean area $< A >$, between the NGRIP previously collected values [Wang et al., 2002] represented by the blue curve and the GRIP ones collected by [Thorsteinsson, 1996] represented by the red curve. Both curves are plotted as a function of the age in years.*

curves, a blue one for NGRIP and a red one for GRIP, plotted as a function of their age. It appears clearly that the sampling rate of the two data sets is not the same. Consequently, only a rough correlation can be seen. This can be explained by the technology evolution, which now enables data sampling with much better precision and accuracy.

The difference in location between the two sites also has consequences on the fabric of the ice, as shown on the figures presented on the appendix A. Indeed, the location of GRIP, on the summit of the ice sheet, compared to NGRIP, that is located on the crest, results in different physical properties that are reproduced in the fabric of the ice of their respective ice cores. At GRIP, ice flows in all directions due to its position at the summit, and to the overlaying ice, which creates a uniaxial compression. The tendency is the same along the whole core, which produces a characteristic fabric, like the ones shown on the figures A.1, A.2, A.3. Typically, the fabrics slowly evolve from a random distribution to a broad single maximum, to end with a stronger single maximum. Oppositely, at NGRIP, the physical properties of the ice core changes with depth due to its position on the crest. This results in some changes in fabrics with depth, as it will be discussed further in the next chapter. Because of the high resolution of the results obtained during this study, the comparison between my results and the ones from

GRIP ([Thorsteinsson, 1996] and [Hansen, 2001]) appears to be impossible. For that reason, in the coming chapter, the results from this thesis will only be compared to the the ones of NGRIP published by Wang *et al.* (2002).

Chapter 5

Results and discussion

In the first part of this chapter, I will present the microstructural and fabric parameters obtained for the warm and the cold period of each of the three studied D.O. events. Then, a comparison between my results and the previous obtained results on the NGRIP ice core will be presented. In the second part, I will describe most of the same parameters, but here, the analysis will focus on the high resolution (down to a 5 millimeters) at high depth (2500 m) Wang *et al.* are compared to the ones of this thesis.
In this chapter, Wang *et al.* (2002)'s results will often be referred to, since they are the newest available data.

5.1 Event analysis: a general tendency

This paragraph shows some plots of the main microstructural and fabric parameters at the D.O. event scale, in order to enable an interpretation of the general evolution of these parameters with depth.

5.1.1 Microstructural results

The mean cross-sectional area $< A >$

The mean cross-sectional area $< A >$ is then calculated from A_k (*c.f.* section 4.1.1). Figure 5.1 displays the crystal area plotted as a function of depth[1] for the NGRIP data collected by Wang *et al.* (2002). The mean areas computed in this thesis are plotted on this graph in order to compare the two data sets. There is a remarkable difference in crystal size between the "warm" period

[1]It is though important to notice that most of the Holocene period, represented by the first 1200 meters of the ice core have been removed since they are not relevant in this project.

of the events comparing to the "cold" one. Besides, this difference increases from D.O. 1 to D.O. 19. In the warm parts of the respective D.O. 1, 8 and

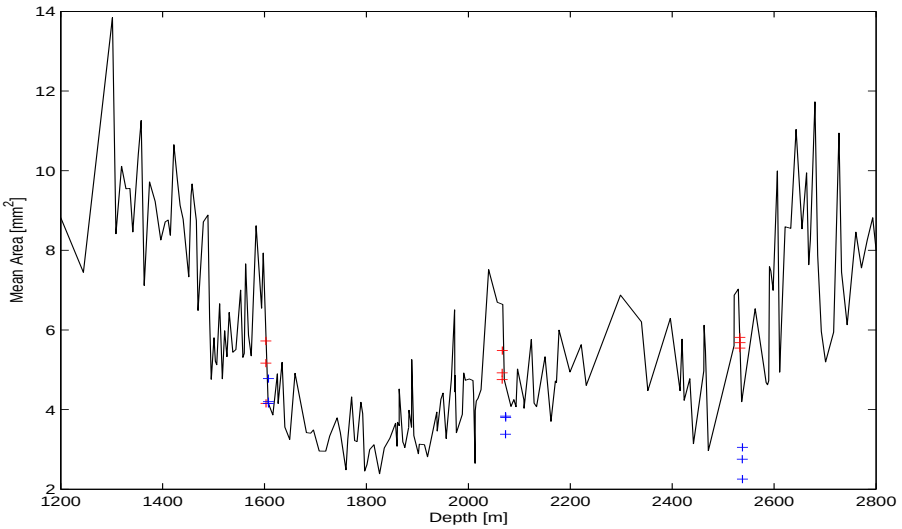

Figure 5.1: *Comparison of the evolution of the mean area $< A >$, between the NGRIP previously collected values [Wang et al., 2002] represented by the black curve and my results, plotted as a function of depth. The red crosses stand for the warm periods of the D.O. events and the blue ones for the cold periods. The three D.O. events are well separated, D.O. 1 at a depth of about 1600 m, D.O. 8 at about 2100 m and D.O. 19 at about 2550 m.*

19, the crystals appear to be growing, whereas they decrease in the cold ones. But overall, there is a good agreement between the discrete data from this work and the continuous data set from Wang *et al.* (2002). However, the crystal areas from the cold parts of the D.O. 8 and 19 are significantly smaller than the ones analyzed by Wang *et al.* (2002). A plausible explanation could reside in the difference in resolution: 8.5 pixel / mm, compared to the 20 pixel / mm in this work.

The mean radius $< R >$

In the coming sections, most of the size related results will be presented as a function of the mean radius $< R >$ in stead of the mean cross-sectional area $< A >$. This choice is made on basis of a close relation between these two parameters, which the next plot, (figure 5.2) clearly confirms. The mathematical relation is simple, $< R >=< \sqrt{A_k} >$ (extracted from the equation 4.1), and is confirmed by the fact that the two graphs (figures 5.1 and 5.2) show the same features.

The crystal size evolutes differently when the warm and the cold parts of

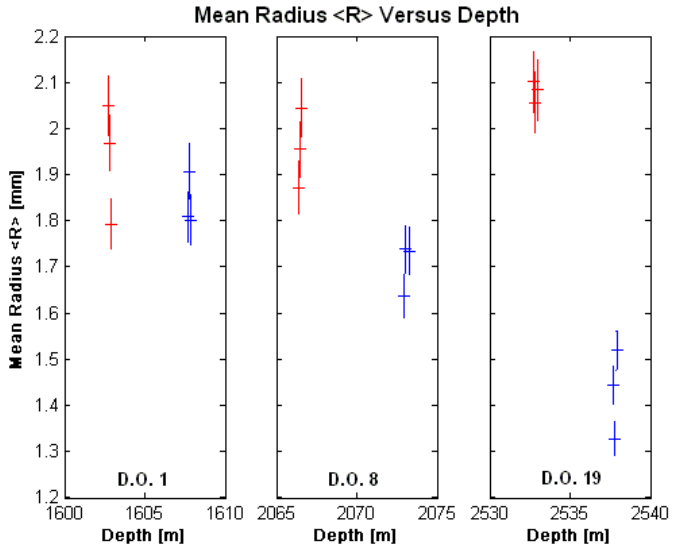

Figure 5.2: *Mean radius $< R >$ for the 3 D.O. events (D.O. 1 - 8 -19). Error-bars representing one sigma .*

the events are analyzed separately and reflect an evolution of the grains size with depth. The grains of the warm periods are roughly constant, despite a slight increase, from an interval 1.8 - 2 mm for the D.O. 1 to about 2.1 mm for the D.O. 19. On the other hand, the grains of the cold periods become smaller (from 1.8 to 1.3 - 1.5 mm). Wang *et al.* (2002) and many others have associated the crystal size with the impurities content.

Impurities and crystal size

Figure 5.3 shows the dust content for each of the D.O. events considered in this paper. Once again, the events are split into two colours, red and blue, respectively representing the warm and the cold part of the events. It appears quite clearly that the low dust content stays almost unchanged for the warm stages, where it increases during the cold stages. A comparison of the trends shown on the figures 5.2 and 5.3 leads to a close relationship between the size of the grains and the dust content. To get closer to this relation, a new plot has been done. The mean impurity content $< D >$ is calculated for the warm and the cold period of each of the three events and is then plotted as a function of the previously calculated mean radii of each thin section. This plot is displayed on figure 5.4. It seems that the data separate in two groups, one when the mean dust content $< D >$ exceeds 1, and another

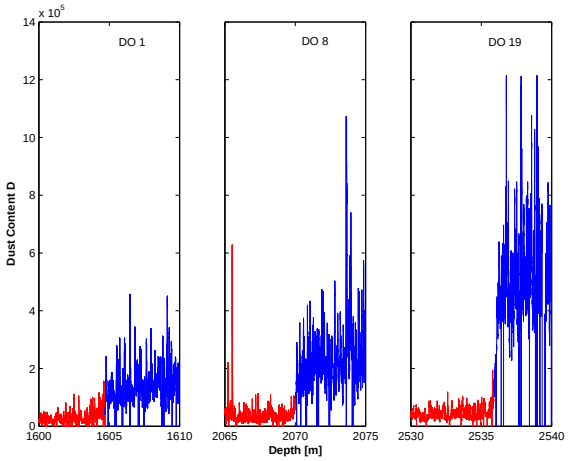

Figure 5.3: *Dust content D for the 3 D.O. events (D.O. 1 - 8 -19). In red, the "warm" parts of the events and in blue, the "cold" ones.*

one when they stay under 1. The second group is typical for grains from ice where the dust content is low, like Holocene ice [Svensson et al., 2003b], and where the normal grain growth process (*c.f.* section 2.7.1) is dominant. The grains grow because they are not disturbed. The figure taken from Thorsteinsson *et al.* (1997), which is shown in the section 4.1 illustrates this process on the ice from GRIP. The first 1000 meters of ice are characterized by grain growth, until the grains reach saturation. In opposition, in the first group, where the dust content increases, the radius of the grains clearly decreases. This observations directly link these two variables again. It is then relevant to investigate the samples at a higher resolution to try to get a better understanding of the relationship between the crystals and the impurities content. This analysis will be presented in the next section, which purpose is try to define the impurities components that control the grains evolution in size, shape and orientation.

The grain shape parameter U

The grain shape, as described in a previous chapter (3.1.3) is determined by the vertical compression U_{zz} and the horizontal shear U_{xz}. Both parameters are shown on the next figure 5.5 for the three D.O. events warm and cold period. On this figure, the values of U_{zz} and U_{xz} are almost the same for the D.O. 1 and 8, where they respectively are about 0.15 and quasi 0. The same parameters are also unchanged when the warm and the cold parts are compared, which means that there is no change in grain shape due to climatic change at that depth (1600 m for D.O 1 and 2070 m for D.O. 8). The zero

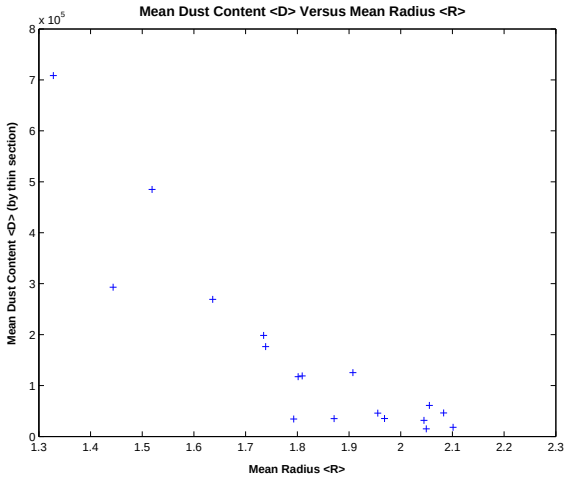

Figure 5.4: *Mean dust content* $< D >$ *as a function of the mean radius* $< R >$ *for the 18 thin sections.*

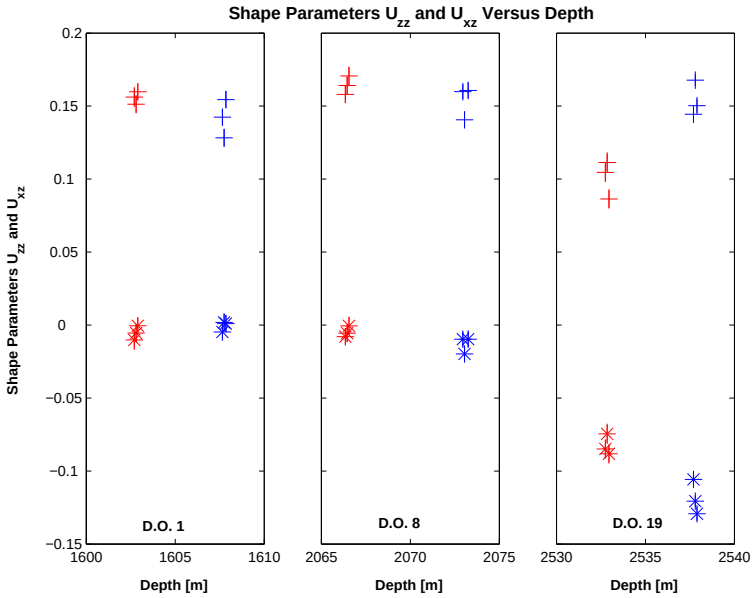

Figure 5.5: *Shape Parameters* U_{zz} $(+)$ *and* U_{xz} $(*)$ *for the 3 D.O. events (D.O. 1 - 8 -19).*

($U_{xz} = 0$) tells us that there is no horizontal shear during the two first events, but only vertical compression represented by U_{zz}. This combination results in elongated horizontal grains. It is known that the vertical stress increases with depth due to the overlaying ice, which let one think that the grains should get flatter and flatter with depth. But the values of U_{xz} and U_{zz} for the D.O. 19 show another pattern. With negative values, $\approx$ -0.75 for the warm part of the event and $\approx$ -1.20 for the cold part, the horizontal shear component U_{xz} has changed compared to the two other events. At the same time, the vertical compression component U_{zz} also have lower value ($\approx$ 0.11 in stead of 0.15) in the warm part, whereas it stays unchanged in the cold part, with a value of about 0.15. The differences in U_{xz} and U_{zz} can be explained by the fact that the grains in the warm periods are subjected to the grain growth process due to the low impurities content that let this process happen. These changes in stresses have an impact in the form of the grains, but also in the form of the fabrics. The grains from the warm part of the D.O. 19 are more round and less tilted than the ones of the cold part. This can be seen when (in absolute values) U_{zz}(warm)<U_{zz}(cold) and U_{xz}(warm)<U_{xz}(cold).

5.1.2 Fabric results

The degree of orientation *R*

Like it has been remarked in the section 4.2.4, the degree of orientation is a conventional parameter that describes the strength of the fabric. The information about the strength of the fabric is given by the magnitude of R, usually shown on the y-axis. The closer to one (or 100%) the values are, the stronger is the fabric. Wang *et al.* (2002) also used this parameter to describe the fabric of their samples. It is important to notice that their sampling method is quite different from the one used in this thesis, and might have significance in the resolution of the data. Their degree of orientation R, is calculated on 200 crystals, which have been randomly and manually picked up in a random area of 5 $\times$ 5 cm (or more for thin sections with large crystals). Oppositely, all the grains of the thin section are taken into account in this work. The next figure (figure 5.6) displays the plot of the continuous degree of orientation as a function of depth[2] obtained by Wang *et al.* (2002). The continuous R from Wang's study increases quasi linearly from a value of about 55% at 1200 m to about 90% at 2800 m, where it behaves asymptotically. This evolution reflects an increasing of the strength of fabric with depth. The degrees of orientation obtained in this thesis, for

[2]Without the Holocene period.

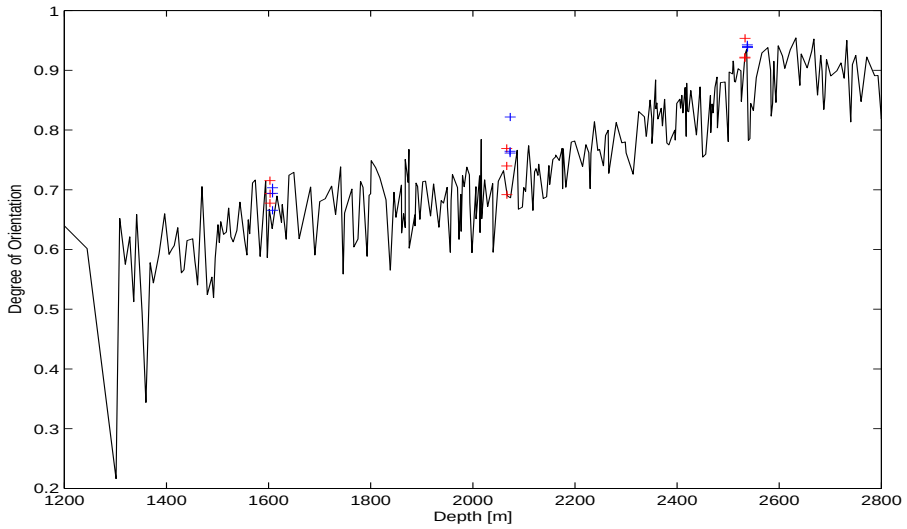

Figure 5.6: *Comparison of the evolution of the degree of orientation R, between the NGRIP previously collected values [Wang et al., 2002] represented by the black curve and my results, plotted as a function of depth. The red crosses stand for the warm periods of the D.O. events and the blue ones for the cold periods. The three D.O. events are well separated, D.O. 1 at a depth of about 1600 m, D.O. 8 at about 2100 m and D.O. 19 at about 2550 m.*

the warm and the cold periods of each of the three D.O. events have been plotted on this same curve. They clearly increase with depth, in both parts of each event and follow the general tendency of the continuous values. This increasing R reflects the changes in the type of fabric, going from the girdle type (D.O. 1 and 8) to the single maximum one (D.O. 19). In other words, the overall agreement is good, however some differences are seen: my results have slightly higher strength of fabric than the ones of Wang *et al.* (2002), for the corresponding depth. The analysis of the previous parameters (grain size and shape) revealed a possible relation between the size and the shape of the grains. Figure 5.5 showed that the smallest grains (the ones from the cold part of the D.O. 19) were smaller and more tilted than the ones of the warm part of the same event. In that case, the degree of orientation is strongly influenced by the size and shape of the grains. Then, the differences of magnitude between my results and the ones of Wang *et al.* (2002) could be explained by the fact that the small crystals manually chosen by Wang *et al.* (2002) are larger than the small grains automatically picked up in that thesis. Therefore, the R computed in that thesis can be higher. One major inconvenient with this R parameter: it only informs about the strength of the fabric, but not about the form of the fabric. This information is gathered

with the second order tensor $\mathbf{a}^{(2)}$.

The second-order tensor $\mathbf{a}^{(2)}$: an expression of the form of the fabric

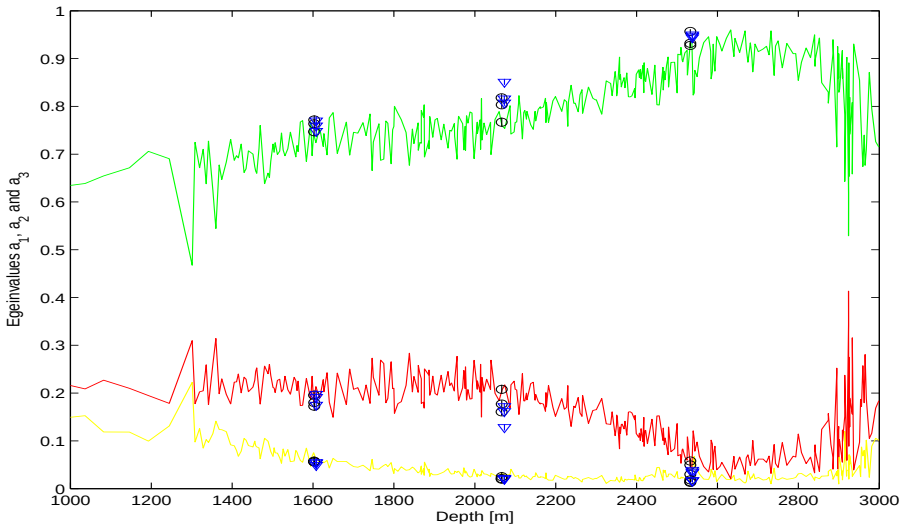

Figure 5.7: *Comparison of the evolution of the three eigenvalues a_1 (green), a_2 (red) and a_3 (yellow), between the NGRIP previously collected values [Wang et al., 2002] and my results, plotted as a function of depth. The black circles stand for the warm periods of the D.O. events and the blue triangles for the cold periods. The three D.O. events are well separated, D.O. 1 at a depth of about 1600 m, D.O. 8 at about 2100 m and D.O. 19 at about 2550 m.*

In this paragraph, the form of the fabric will be analyzed. Figure 5.7 represents the plot of the continuous eigenvalues from Wang *et al.* (2002) as a function of depth. Each colour stands for an eigenvalue. The eigenvalues a_2 (red) and a_3 (yellow) are generally decreasing, from 0.2 to 0.05 for a_2 and from 0.1 to 0.05 for a_3 to a depth of about 2600 m, where they are nearly equal. From 2600 to 2900 m, they both keep the same low value; then, they raise again to much higher values. Oppositely, a_1 (green) logically increases to respect the relation cited before[3] ($a_1 + a_2 + a_3 = 1$). a_1 goes from about 0.6 to almost 0.95 at 2600 m, from where it falls again. The calculated eigenvalues from this project are then shown on the same graph in order to establish a comparison. The blue triangles stand for the cold periods of the three events and the black circle for the warm ones. As mentioned above, the second-order tensor informs about the form of the fabric. Wang *et al.*

[3]See section 4.2.5.

(2002) separated the NGRIP ice core in 5 main fabric groups, a random fabric for the first 800 m, a broad single maximum from 800 to 1400 m, a girdle fabric from 1400 to 2500 m, a strong single maximum between 2500 and 2800 m and a single maximum from 2800 to the bottom. In a random fabric, the plot of the c-axis do not show any special pattern, which results in a Schmidt plot with dots all over. It is a typical fabric found in the firn. The broad single maximum describes a fabric with a concentration of dots in broad circle-like in the middle of the plot. This type stands for the ice that is under the influence of a slight vertical compression. The girdle fabric typically shows a broad line of plots on the Schmidt diagram. This fabric is the result of the combination of the physical position of NGRIP (on a crest) and the increasing vertical compression due to the overlaying ice. The ice is forced to flow along the sides of the crest, resulting in the girdle fabric. The strong single maximum fabric, represented by a strong concentration of c-axis around the middle of the diagram is probably due to the increasing horizontal shear, resulting from the flowing of the ice. Finally, the single maximum fabric, that reflects the change in stresses at the bottom, due to the melting at the bottom that reduces the effect of the horizontal shear.
The three D.O. events (1, 8 and 19) selected for this project have respectively the following depth, 1600, 2100 and 2550 m. From these facts, the observed fabrics should be, according to Wang *et al.* (2002) a girdle fabric for the two first D.O. events and a strong single maximum for last one. This hypothesis is verified by the values of $\mathbf{a}^{(2)}$ observed on figure 5.7. As mentioned on section 4.2.5, the typical girdle fabric would imply the relation $a_1 \approx a_2 > a_3$. In our case, $a_1 > a_2 > a_3$, which explains the broad bands displayed on the Schmidt plots of the D.O. 1 shown on figure 5.8. For the D.O. 8 (figure 5.9), the fabric is also a girdle one, but the central band is a bit narrower, which is the consequence of a slightly higher $a_1^{(2)}$, compensated by some lower $a_2^{(2)}$ and $a_3^{(2)}$. The strong single maximum fabric only appears for the D.O. 19, when $a_1^{(2)} > a_2^{(2)} \approx a_2^{(2)}$. The form of the corresponding fabric is displayed on figure 5.10. When observing the Schmidt plots of the three events, it appears that the fabrics from the cold and the warm periods of the events do not show any notable change. This was to be expected since the fabric is the result of the physical processes of the ice sheet, which is a long time variation process. This is in opposition to the short time variations that the climatic events represent. The reason why the fabric changes suddenly from a girdle type to the strong single maximum is not completely understood. In other ice cores, like at GRIP, the strong single maximum as been interpreted as the result of the uniaxial vertical compression. But at NGRIP, the vertical compression is accompanied by an increasing horizontal shear with depth,

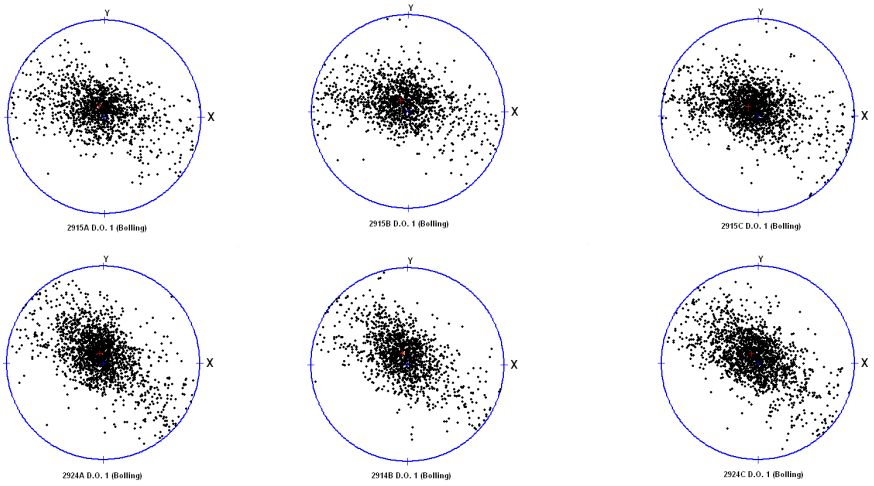

Figure 5.8: *Schmidt plots for the Dansgaard-Oeschger (D.O.) event 1 (Bølling) [thin sections 2915A-B-C and 2924A-B-C].*

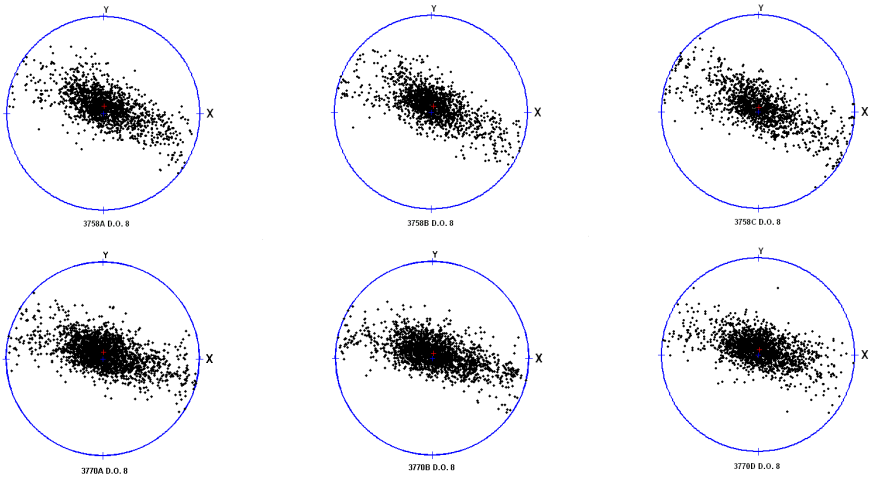

Figure 5.9: *Schmidt plots for the Dansgaard-Oeschger (D.O.) event 8 [thin sections 3758A-B-C and 3770A-B-D].*

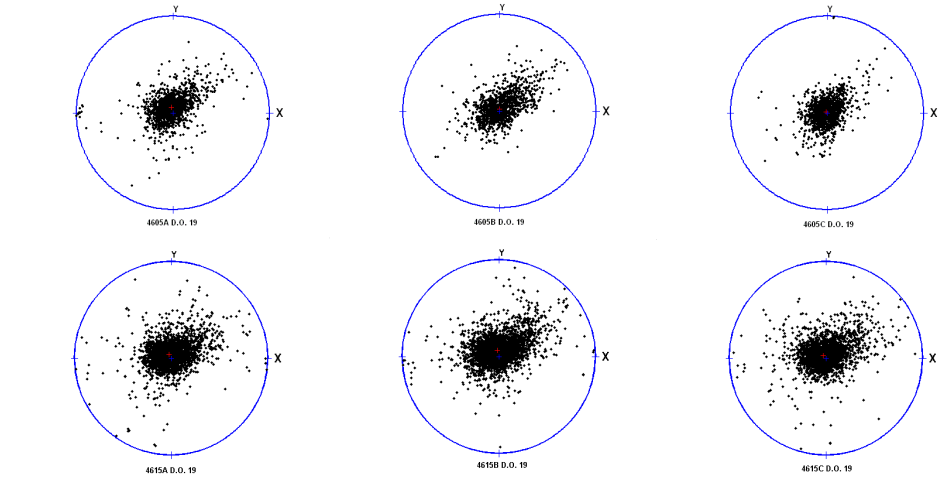

Figure 5.10: *Schmidt plots for the Dansgaard-Oeschger (D.O.) event 19 [thin sections 4605A-B-C and 4615A-B-C].*

due to the stronger and stronger flow lines along the crest. In other words, the horizontal shear increases with depth. Consequently, the transition from the girdle to the single maximum fabric could be explained by this process in the interval 2600 to 2800 m.

5.1.3 Comparison between microstructure and fabric

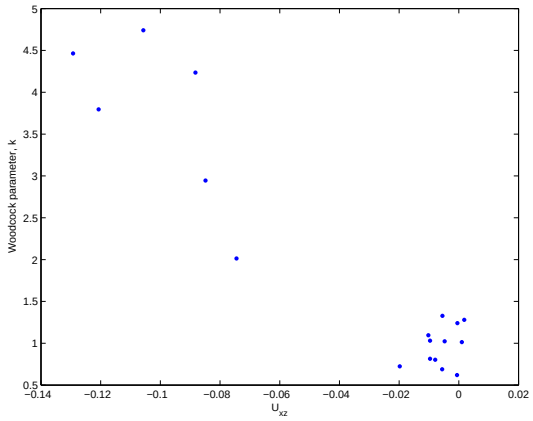

Figure 5.11: *Woodcock parameter as a function of the horizontal shear component U_{xz} for the 18 thin sections.*

Two of the described previous parameters, *i.e.* the second-order tensor

$\mathbf{a}^{(2)}$ and the grain shape parameter U can be plotted one against the other to show the correlation between the horizontal shear component U_{xz} and the fabric of the ice. This relation can be observed if the second-order tensor's components are expressed by the Woodcock parameter, k (see equation 4.8). This later k is then plotted as a function of U_{xz} for each of the 18 thin sections, as shown on figure 5.11. The relation between these two parameters seems to be quite linear, which means that the fabrics are directly related to the stresses. When $k> 1$, it means that the fabric is of the single maximum type, and oppositely, when $k< 1$, the fabric is of the girdle like type. On figure 5.11, $k>1$ when $U_{xz}\neq 0$, which means that the fabric is turning to a single maximum. The six dots on the left of the graph represent the six thin sections of the D.O. 19, where the fabric is single maximum. The 12 others, on the right lower corner stand for the D.O. 1 and 8 and represent a girdle fabric.

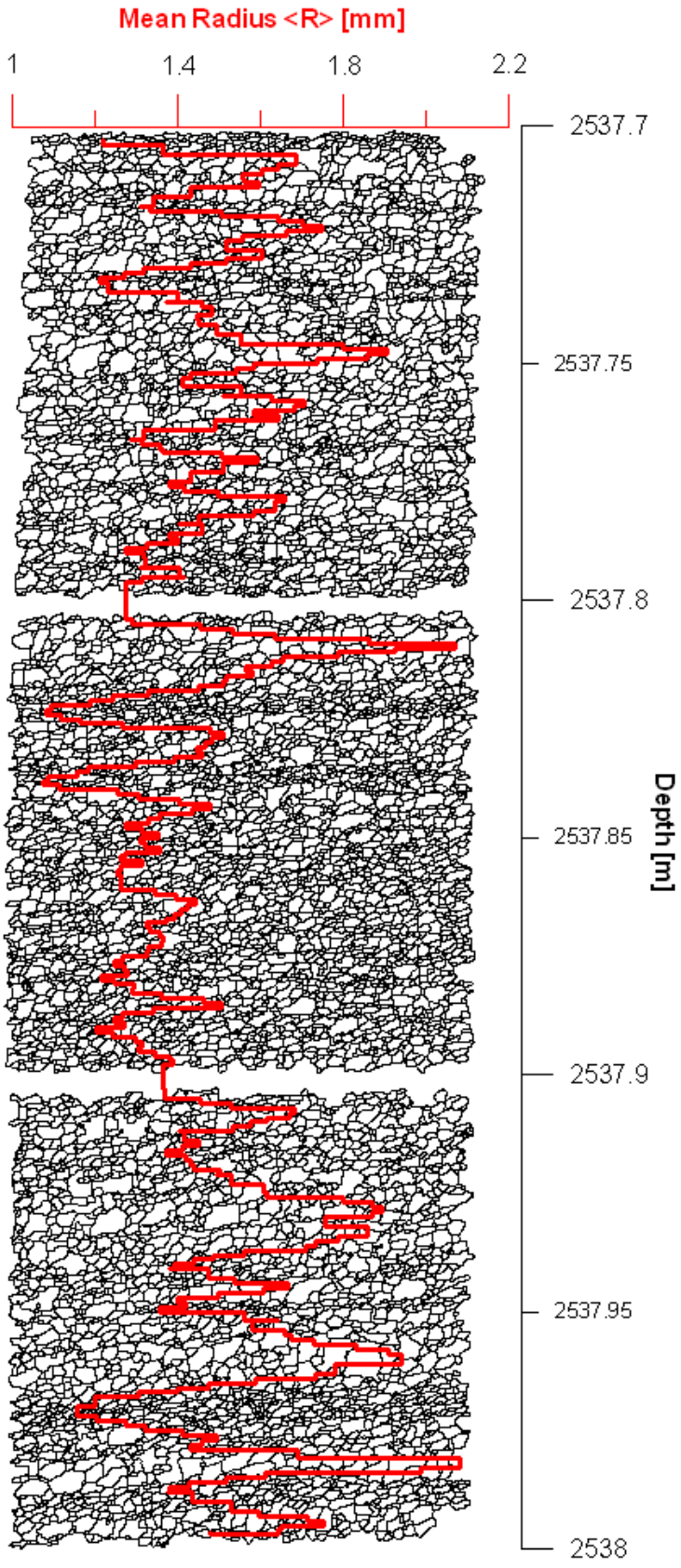

Figure 5.12: *Mean Radius < R > on thin sections 4615A -B -C 's outlines (D.O. 19).*

5.2 5mm resolution: a detailed analysis

5.2.1 Microstructural results

The graph shown on figure 5.12 displays the calculated continuous mean radius $< R >$ for the three thin sections of the cold period of the D.O. 19, plotted on the microstructures of the same thin sections. The gaps between the microstructures have two practical explanations: the width of the saw from the bandsaw (about 1 mm), and the selection made during the control of the microstructures. Indeed, during this check, the border grains that did not appear in full size have been rejected in order to not spoil the calculations of the areas of the grains. This graph reproduces the high resolution of the performed measurements and clearly shows variations in grain size represented by bands of smaller and larger grains. These same bands alternate and could reproduce the seasonal variations; the small grains representing the summer and the large ones the winter (due to the higher impurity concentration in summer than in winter [Svensson et al., 2005]). These variations of grain size on the outline are confirmed by the changes in mean radius that is computed by the *Texture toolbox*. The continuous mean radius plot follows perfectly the bands apparent on the outlines. The next question is: are these variations in mean radius significant? To control that, a new plot displaying the mean radius and its standard deviations for a chosen thin section must be shown (see figure 5.13). On this figure, the mean radius $< R >$ varies a lot, from about 1.3 to 2.7 mm at the depth of 2537.98 m (1.4 mm of amplitude), while the curves representing 1 sigma and 2 sigma have a respectively a maximum amplitude of about 0.2 and 0.4 mm at the same depth. Consequently, the variations of the computed radii are significant, which is important since either the mean radius or the radius alone will be displayed in nearly all the coming plots.
The first part of this chapter (section 5.1.3) showed that the grain size and the impurities content were closely related at the thin section scale. In the next section, the relation between impurities content and crystal size will be deepened by analyzing the mean radius evolution at a 5 mm resolution.

Impurities and crystal size

Some of the previously extracted chemical components[4], such as the dust content, the calcium, the nitrate, the sodium and the sulfate concentrations are, together with the mean radius, plotted as a function of the depth (figure 5.14). The choice of the thin sections 2924A-B-C (cold part of the D.O. 1)

[4]Collected by the Continuous Flow Analysis method (C.F.A.).

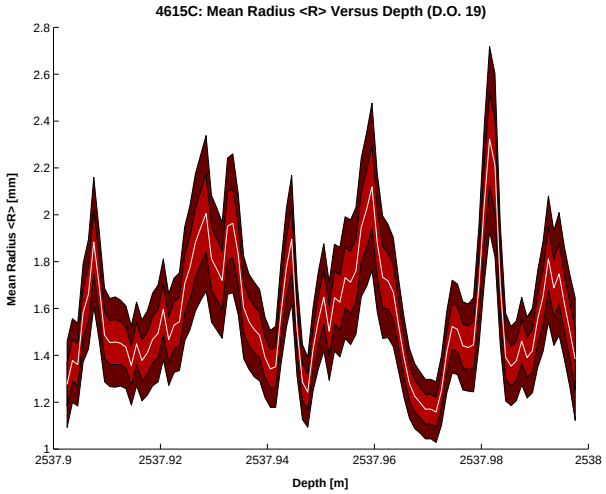

Figure 5.13: *Mean Radius $< R >$ and the standard deviations (sigma) on thin section 4615C 's outlines (D.O. 19) as a function of depth. The thin white line in the middle is the mean radius, the darker orange envelope around it represents 1 sigma and the brown envelope 2 sigma.*

in stead of the one from the D.O. 19, like in most of the times in this chapter, is explained by the fact that the chemical components do not all have continuous available data for all the sections. Therefore, the 2924 sections are more suitable to compare the chemical components with the mean radius since they provide continuous data. The idea is behind this plot is to try to correlate the mean grain size and the impurities content, in order to find which of the chemical components mostly influences the crystal size. It is though necessary to precise that the resolution of all these components is not the same, which results in some curves that look more smoothed than some others. But since the variations of the concerned curves are big enough to accomplish the comparison, these differences in resolution should not be ignored. The figure 5.14 clearly shows that the same peaks appear simultaneously for all the plotted components (despite very different amplitudes), and that they correspond to a fall in the mean radius size. Three of these peaks are marked on the plot by the dashed lines. The fact that the peaks are simultaneous does not help us in the determination of the most determinant chemical component. A better way to analyze this impurities/radius relation must be found.
It has just been established that the crystal size and the impurities content were strongly related at the thin section scale. If now the two curves from the figure 5.14, representing the mean radius and the line scan intensity, are isolated as presented on figure 5.15, they can evidently be anti-correlated.

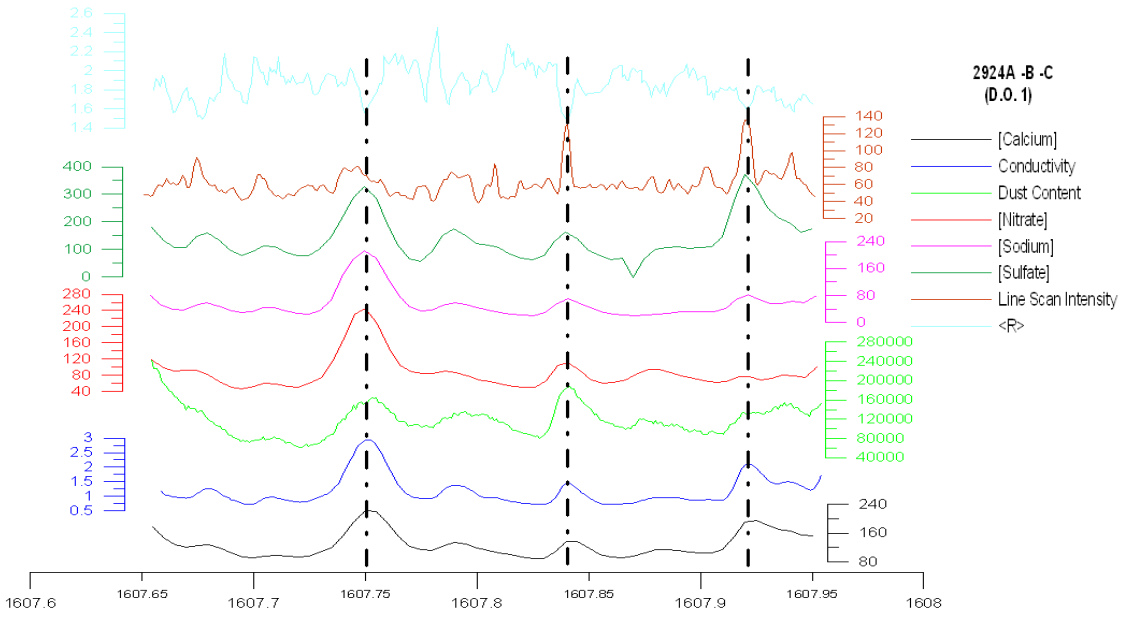

Figure 5.14: *Plot of different chemical components and mean radius $< R >$ for the thin sections 2924A-B-C (D.O. 8) as a function of depth.*

It is known that the line scan intensity also reflects the impurities content [Svensson et al., 2005]. When the ice is "clean", it appears dark and the scan intensity is low, in opposition to the "dust rich" ice, represented by lighter bands with higher intensity. These two curves sensibly have the same resolution, and permit to deduce that the mean radius $< R >$ is strongly related to the impurities content, also at the 5 mm scale. Each dash line show the most prominent peaks in the line scan intensity and their corresponding low values of mean radius .
Next, a chemical component (the calcium for example) is chosen in order to analyze its influence on the separated warm and cold periods on the D.O. events. To accomplish that, the calcium concentration is plotted as a function of the mean radius for the D.O. 1 and is displayed on figure 5.16 below. The first apparent pattern resides in the separation of the data into two different groups according to the event period (the blue group for the cold period and the red one for the warm one). This feature pushes one to conclude that the calcium cannot be the only determining parameter since one mean radius corresponds to more than one calcium concentration. A fit line for each period has been added to study the reliability of the data. Their respective equation is written in the corresponding colour on the side of the

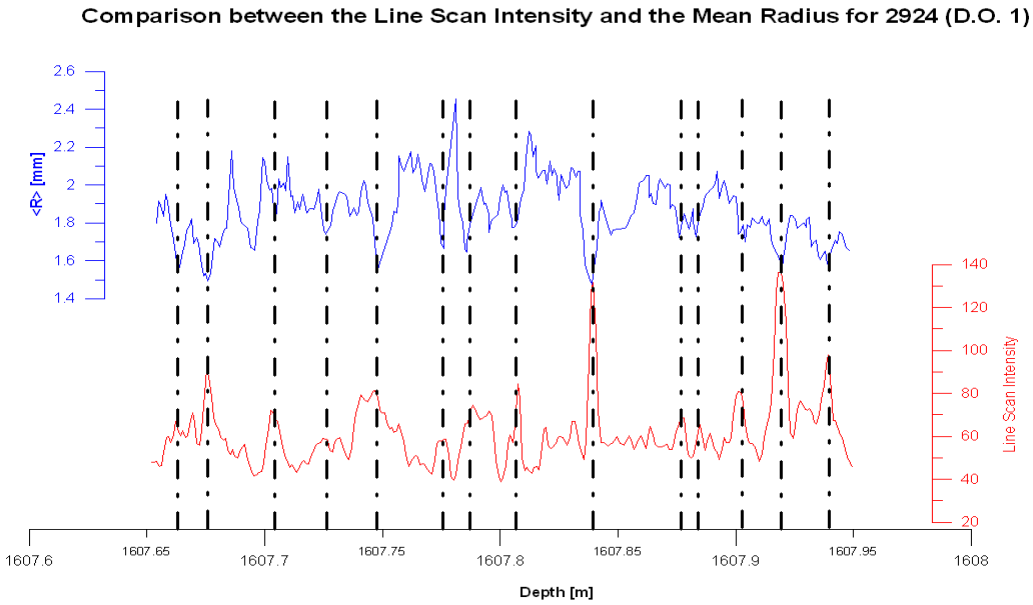

Figure 5.15: *A close up to the anti-correlation of the mean radius $< R >$ and the line scan intensity, for one thin section: 2924 (D.O. 1).*

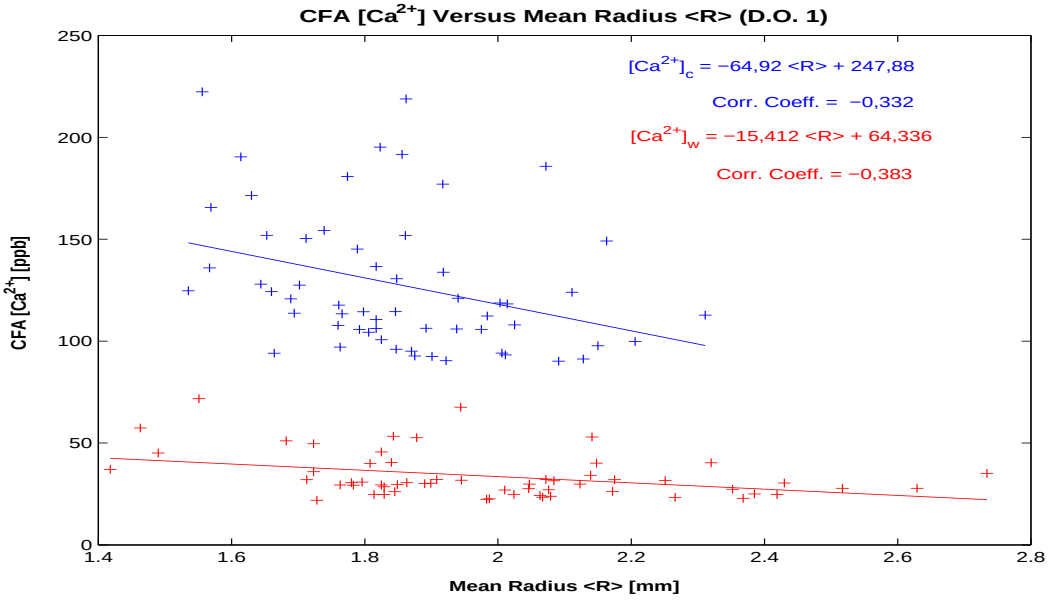

Figure 5.16: *The calcium and mean radius correlation for the D.O. 1. The blue dots represent the plots of the concentration for the cold period of the D.O. 1, and the red the ones for the warm one.*

curves. Then, a correlations coefficient[5] has been calculated and notified on the figure. The sign of the coefficient informs about the slope direction of the fitting line. When negative, the mean radius increases with decreasing calcium concentration. Here, the coefficients are low and almost equal (≈ -0.3), which reflects a relatively bad correlation. Sometimes, data need to be plotted differently to show features that can be interpreted. The last plot did not enable any constructive correlation between the two parameters; therefore, a new plot of the same data set is following. This time, it will represent the logarithmic function of the calcium concentration as a function of the mean radius $< R >$ for the 3 D.O. events together. This plot is displayed on figure 5.17 shown below. The data are still appearing separated, even though the

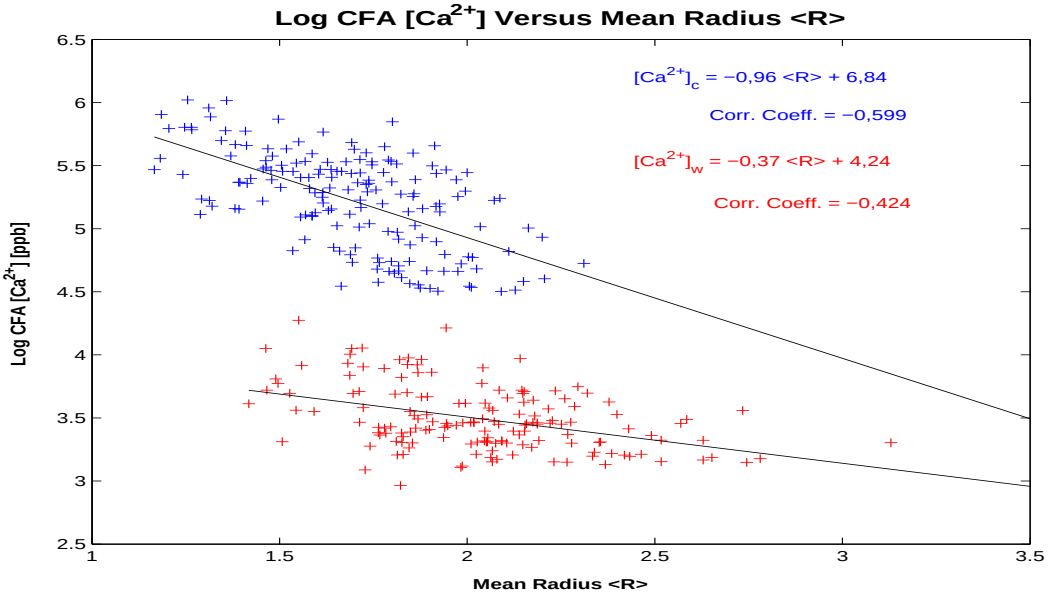

Figure 5.17: *The log of the calcium and mean radius correlation for the 3 D.O. together. The blue dots represent the plots of the concentration for the cold periods, and the red the ones for the warm ones.*

correlations coefficient got better: from 0.4 for the one of the warm period and from 0.6 for the one of the cold period. But again, one single mean radius corresponds to several calcium concentrations, even inside the separated periods. From these observations, it is obvious that the size of the grains do not only depend on the concentration in calcium. Moreover, it also indicates

[5]Normalized measure of the strength of the linear relationship between two variables: uncorrelated data results in a correlation coefficient of 0, while equivalent data sets have a correlation coefficient of 1

that, whatever the D.O. event that is chosen, the D.O. 1 on figure 5.16 or the three D.O. together on figure 5.17, the same pattern is obtained. Many other graph displaying each chemical component as a function of the mean radius $< R >$ could be done in order to try to determine the component that influences the most the grain size. But to reduce the number of plots, a table (table 5.1) resuming the correlation coefficients of the linear fits between all the chemical component concentrations (Ca^{2+}, NO_3^-, SO_4^{2-}, Na^+) plotted as

Event	$[Ca^{2+}]$	$[Na^+]$	$[NO_3^-]$	$[SO_4^{2-}]$
D.O. 1 (Warm)	-0.383	-0.002	-0.410	-0.298
D.O. 1 (Cold)	-0.332	-0.186	-0.183	-0.384
D.O. 8 (Warm)	-0.634	-0.129	-0.604	-0.628
D.O. 8 (Cold)	-0.423	-0.263	-0.302	-0.229
D.O. 19 (Warm)	0.090	0.186	0.210	0.183
D.O. 19 (Cold)	-0.459	0.180	0.302	-0.003

Table 5.1: *Table presenting the different chemical components concentration correlation coefficients, separated in the warm and cold part of each D.O. event.*

a function of the mean radius is shown. Some of the values from this table must be rejected, for different reasons. The lowest correlation coefficients (≈ 0) such as the ones of the sodium of the warm period of the D.O. 1, the calcium of the warm period of the D.O. 19 or the sulfate of the cold period of the D.O. 19 have to be ignored because they cannot lead to any correlation. The same remark for the events which have a large difference between the coefficients from the cold and the warm periods: *e.g.* the ones of the concentrations of calcium, nitrate and sulfate from the warm part of the D.O. 8, reach over 0.6, but have unacceptable values from the cold part of the same event.

From this section, it seems to be relatively difficult to find the influence of each impurity on the size of the grains, since almost all the components evolutes in the same way. Consequently, it might be a good idea to try to find out how these impurities act on the crystals size more than which of them plays a role on the grain size. The impurities have been separated in two groups (as explained in the section 2.7.1): the soluble particles (*e.g.* Ca^{2+}, NO_3^-, SO_4^{2-}, Na^+)and the insoluble ones (dust). These two types of impurities have different roles in the crystal growth processes, and influence therefore the distributions of the radii of the grains. This influence can be detected by analyzing the standard deviations on the radius of the grains.

The radius distributions

Any experimental work must contain a statistical part informing about the significance of the analyzed data. It is therefore important to know how the data are distributed. The coming three graphs (figures 5.18, 5.19 and 5.20) will present the plot of the distributions of the computed radius R_k for each single crystal of each of the D.O. event studied in this project. In many cases, the distributions are *normal distributions* (also called the Gaussian distribution). They occur in many situations, when there is a large number of small effects acting additively and independently. In our case, the distribution do not have the typical "bell shape" of the Gaussian distribution. From that observation, the best distribution type must be found. The three

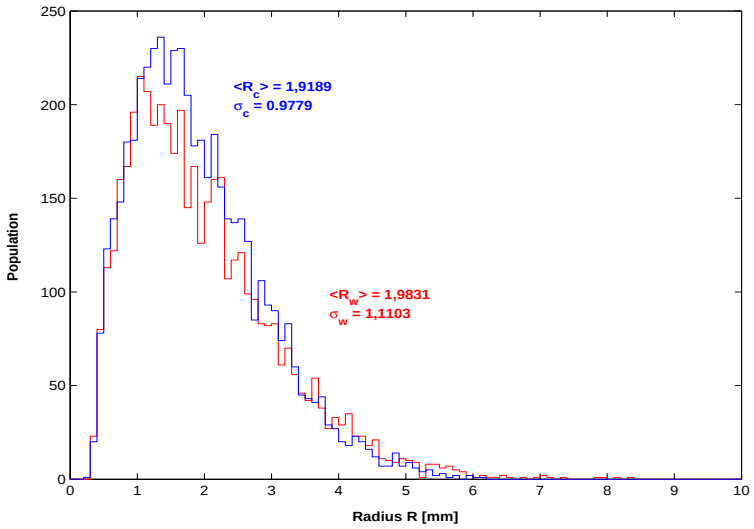

Figure 5.18: *Step-plot of the radius R (Raw data) for the event D.O. 1. The red curve represents the "warm" period of the event and the blue one, the "cold" one.*

figures named above all show the same pattern, a "bell-like form with a kind of tail", that can be explained by the fact that sometimes, data can act as multiplicative (rather than additive). In that case, the assumption of normality is not justified, and it is the logarithm of the variable of interest that is normally distributed. Then the variable is distributed according to the following equation 5.1:

$$f(R) = \frac{1}{R\sigma\sqrt{2\pi}} e^{\frac{-(ln(R)-\mu)^2}{2\sigma^2}}, \tag{5.1}$$

where R represents the radius, σ, the standard deviation and μ, the mean radius (normally noted $< R >$ in this work). The distribution of the directly observed variable is then called *log-normal*. In their respective works

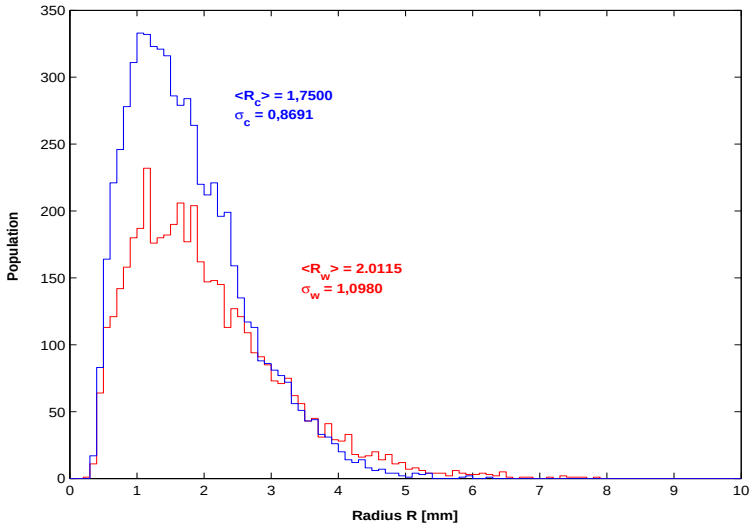

Figure 5.19: *Step-plot of the radius R (Raw data) for the event D.O. 8. The red curve represents the "warm" period of the event and the blue one, the "cold" one.*

on GRIP, Thorsteinsson (1996) and Hansen (2001) also found their crystals areas distributed according to the log-normal definition, which confirms the results on this work. On the figures 5.18, 5.19 and 5.20, the mean radius $< R >$ and the standard deviation σ for each period (cold and warm) of each D.O. event is noted. These three graphs enable to gather information about the differences in population together with the differences in crystal size at two different time scales; the variations within the events (the cold and the warm period of each event) and the variations between the three D.O. events. Finally, they also inform about the differences in standard deviations on the mean radius $< R >$ for each period of each D.O. event (written on each plot).

These plots confirm previous hypothesis concerning the evolution of the grain size with depth *i.e.* the small crystals from the cold periods are getting smaller with depth while the larger crystals from the warm periods that are getting slightly larger (c.f. figure 5.2). This phenomenon has until now been explained by the normal grain growth process, which takes place in the warm parts of the events, where the impurities content is lower (c.f. figure 5.3). But it seem that another process limits the crystal growth in the cold parts of the events. Alley (1992) suggested that the rotation recrystallization process (see section 2.7.2) was responsible of this stop in grain growth. But the role of the insoluble impurities should not be forgotten. In fact, the pinning [Alley et al., 1986] of the grain boundaries by the dust also seems to be responsible of this stop in grain growth. Since the dust concentration

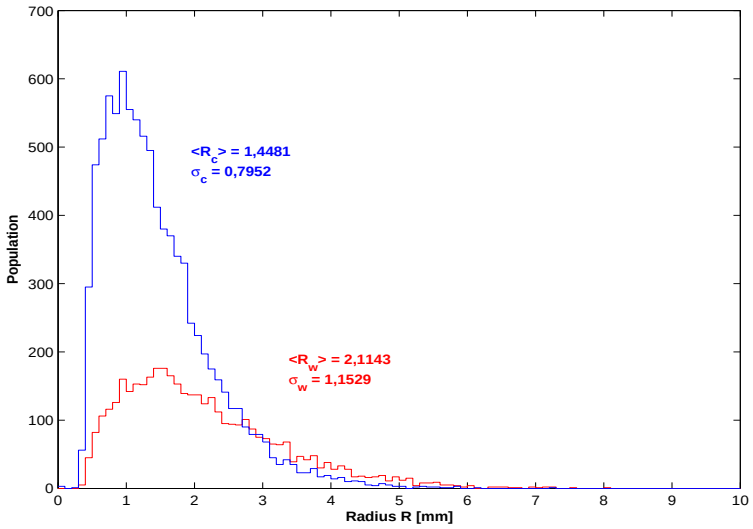

Figure 5.20: *Step-plot of the radius R (Raw data) for the event D.O. 19. The red curve represents the "warm" period of the event and the blue one, the "cold" one.*

influences the distribution of the radii of the grains, it must also influence the standard deviations. In other words, if the standard deviations are not constant in the three studied D.O. events, it must be explained by the pinning process. Figure 5.21 indicates clearly that the standard deviations are different, both within the same event, but also at the larger scale, between events. This difference actually increases with depth since the deviations of the D.O. 19 have an amplitude of almost 0.4 mm, against 0.2 mm for the ones of the D.O. 1. This is probably due to the higher impurities concentrations on the D.O. 19 than on the D.O. 1 (see figure 5.3).

5.2.2 Fabric results: Variations at the 10 cm scale

A summary of the fabric evolution from event to event is shown on figure 5.22. Two main features can be observed on that plot: the general tendency of the eigenvalues $a_1^{(2)}$, $a_2^{(2)}$ and $a_3^{(2)}$ values evolution and their amplitude evolution. Generally, $a_1^{(2)}$ is increasing linearly from D.O. 1 to D.O. 19, which results in a decreasing of the other eigenvalues $a_2^{(2)}$ and $a_3^{(2)}$. At the same time, the amplitude of the covered interval get also smaller with depth. These features reflect the two different types of fabric, girdle and single maximum, that have been mentioned before. The reduction of the intervals of amplitude reveals a much stronger fabric toward the bottom of the ice core. These later observations are showing that the fabric evolves from event to event, but do not allow to interpret fabric changes at the seasonal scale.

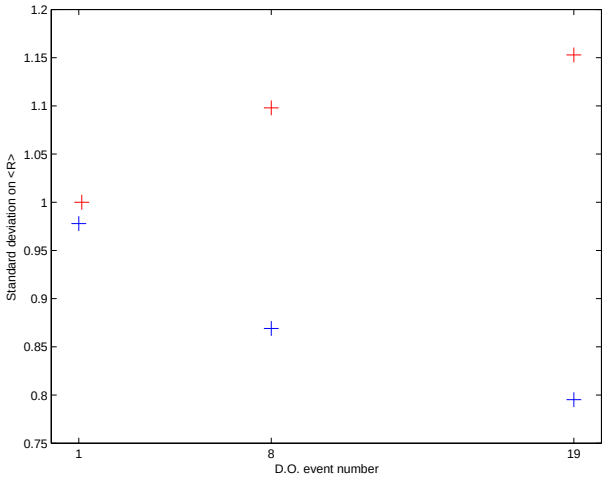

Figure 5.21: *Standard deviations σ for the cold (blue dots) and the warm (red dots) periods of each of the D.O. events.*

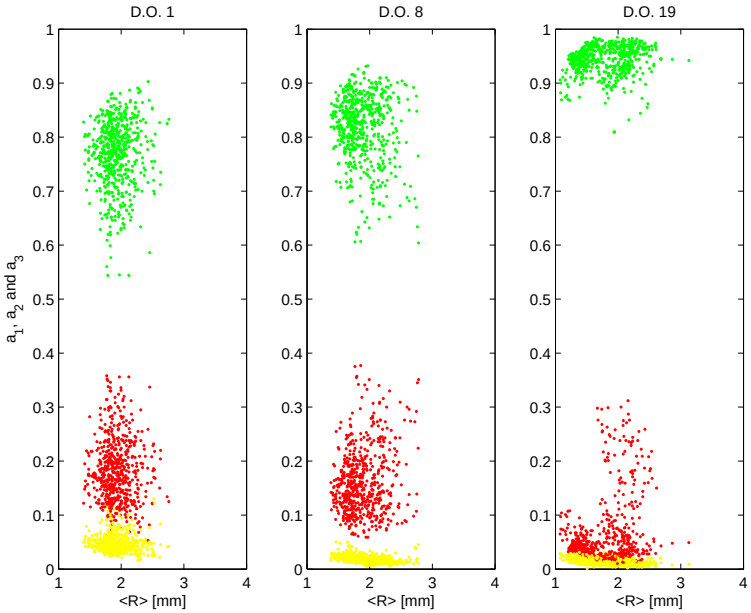

Figure 5.22: *Orientation distribution represented by the eigenvalues a_1 in green, a_2 in red a_3 in yellow for each event as a function of the mean radius $< R >$.*

Previous authors already investigated the relation between the crystal size and the fabric. Svensson *et al.* (2003) noted that an analysis of the R (degree of orientation) parameter of the ice of the Holocene (at a depth of about 301 m) fluctuated but could not be correlated to any other parameter. From that, they concluded that the fabric did not show any seasonal variation at that depth. The next presented graph (figure 5.23) represents the outline (or mask) of the thin section 4615C, from the D.O. 19. On that picture, the mean radius, $< R >$ and the three eigenvalues, $a_1^{(2)}$, $a_2^{(2)}$ and $a_3^{(2)}$ are plotted. On the 10 cm thin section, radical changes in crystal size, represented by the bands of large and small grains are visible. Four bands of smaller crystals are sharply defined (at the depths of about 2537.91 - 2537.94 - 2537.97 and 2537.99 m), whereas it is possible to distinguish one more at the depth 2537.95 m. The important information on that plot is that it shows that the second-order tensor values evolutes according to the grain size. When the grains are small, $< R >$ is obviously small, but $a_1^{(2)}$ is also decreasing which is compensated with a increasing in $a_2^{(2)}$, while $a_3^{(2)}$ almost stays unchanged. This is characteristic of the girdle like fabric. Oppositely, in the bands of bigger grains, the fabric is of the single maximum type ($a_1^{(2)} > a_1^{(2)} = a_1^{(2)}$). These synchronized changes represent an evolution of the fabric with the grain size at a high resolution scale, but do not correspond to the modeled annual layers obtained by the ss09sea model [Johnsen, 2002]. This model suggests that the annual layers at that depth are about 0.6 mm thick, which should correspond to a total of 16 years on the shown thin section. On the figure 5.23, counted bands enable to detect 6 or maybe 7 cycles, which obviously do no represent the annual variations. What they really represent is not known and will not be studied in that project. But it is relevant to notice that similar observations have been done by Hansen *et al.* (2002) on the GRIP ice core. He observed different degrees of orientation on the cloudy bands (85%) and on the bright ice (91%) of a thin section.

5.2.3 Comparison between microstructure and fabric

The observations above concerning the changes in fabric within the 10 cm thin section (4615C in this case) can be further analyzed. A graph displaying the Woodcock parameter, k, plotted as a function of the mean radius $< R >$ (for 4615C), is shown on figure 5.24. The plot tells us that the zones presenting the small grains are close to a girdle-like type of fabric ($k \approx 1$), and that the ones presenting larger grains are of the single maximum type. The appearing linear relation is quite rough, but sustains the fact that the

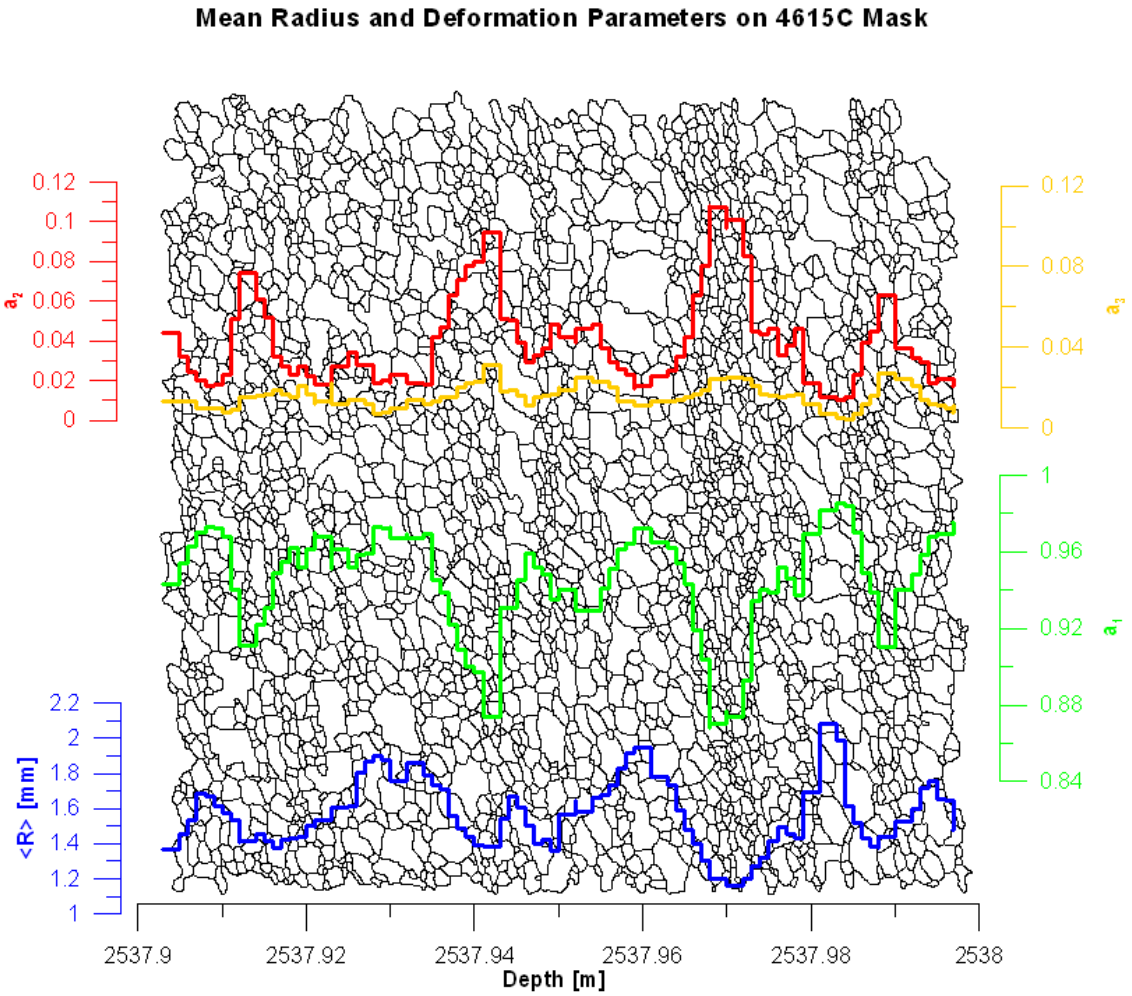

Figure 5.23: *Deformation parameters a_1 in green, a_2 in yellow and a_3 in red for each event versus the mean radius $< R >$ in blue.*

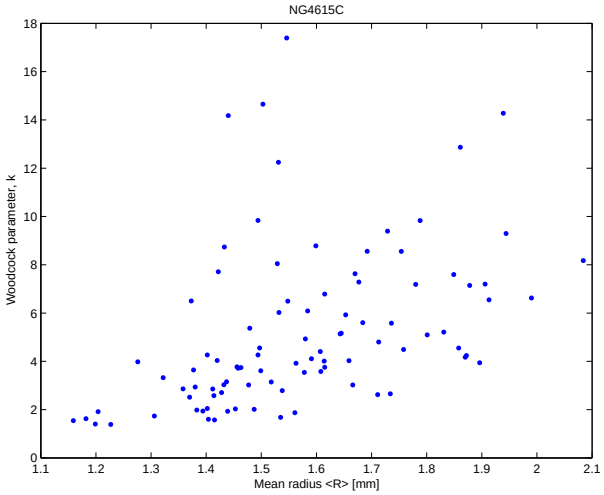

Figure 5.24: *Woodcock parameter k plotted as a function of the mean radius* $< R >$ *for all the crystals from the thin section 4615C.*

smaller the grains are, the more oriented the fabric is. In other words, the small grains are more subjected to stress changes than the big ones.

Chapter 6

Conclusion

This master thesis has presented an analysis of the texture (microstructure and fabric) of the ice crystals from three selected D.O. events of the NGRIP ice core (D.O. 1, 8 and 19). This work has been accomplished in the continuity of previous recent works done on ice crystals from ice cores from Greenland. Thorsteinsson (1996), studied the texture of the grains along the whole GRIP ice core, while others like Hansen (2001) chose to concentrate their study on single events, D.O. 3 in his case. The same studies have been done on NGRIP, Wang *et al.* (2002) analyzed the general tendency of the texture along the whole core, while Svensson *et al.* (2003a and 2003b) chose to analyze single events.
In this work, the three intervals have been carefully chosen, in order to avoid the transition periods, which enabled the comparison of the two different periods, the stadials and the interstadials of each D.O. event. The obtained results are comparable to the ones obtained by the above cited authors. The fabric at NGRIP is changing gradually with depth, going from a girdle fabric (D.O. 1 and 8) to a strong single maximum (D.O. 19). This change in fabric corresponds to a change in stress. On the upper part of the core, the ice is only influenced by the uniaxial vertical compression, and results in the girdle fabric. Further down, at about 2500 m, the horizontal shear appears as a result of the ice flow; then, the fabric becomes of the single maximum type. At this point, the flow influences the fabric and vice-versa, it can be talked of interdependency. But the stresses are not the only parameters that influence the crystals fabric and microstructure. It has been shown that the impurity content had a determinant role too. When ice is not submitted to stress and has a low impurity content, the grains are just growing, obeying the law of *normal grain growth*; this process is typical for the Holocene ice [Svensson et al., 2003b], but also occurs deeper. Indeed, it has been seen in the warm parts of the three studied D.O. events, where the dust content is

much lower than in the cold parts. In the cold parts, the grains have been found smaller, resulting from three processes: the *rotation recrystallization*, the *pinning* of the grain boundaries by the insoluble impurities and the influence of the soluble particles. The *rotation recrystallization* subdivides the existing grains into newer grains [Alley, 1992], while the *pinning* limits the grain growth [Alley et al., 1986] and [Weiss et al., 2002]. In both cases, the grains appear small. This work showed that both acted on the grain size evolution. The analysis of the soluble impurities has also revealed an influence on the grain size evolution. Most of the chemical components showed the same correlation with the radius evolution: the high impurities concentrations correspond to the smallest grains. It is therefore difficult to get any relevant information with these impurities. Finally, some changes in fabric have been observed at the thin section scale, at a high depth (2550 m), which constitutes a new observation in ice crystals studies. It has also been established that the visible bands and their corresponding fabric did not reflect the seasonal variations, since the number of counted layers did not match the predicted annual layers that Johnsen (2002) modeled. Consequently, the signification of the observed layers is unknown at the moment. The initialization of the micro-folding process that disturbs the stratigraphy towards the bottom of the ice core [Svensson et al., 2005] could be a plausible hypothesis.

A further study of a continuous fabric evolution at high depth might be helpful to gather important information concerning the influence of the folding on the stratigraphy and on the crystals microstructure and fabric.

Appendix A

GRIP fabrics

The next figures are representing the Schmidt diagrams for the GRIP data. They cover the whole core and show a typical fabric evolution for a core that is located on the summit of a crest, which results in an uniaxial compression. The fabric goes from a random distribution beginning at the top of the core to a depth of about 1500 m (figure A.1) to a broad single maximum, from about 1500 m to about 2000 m (figure A.2), where they finish in a narrow single maximum.

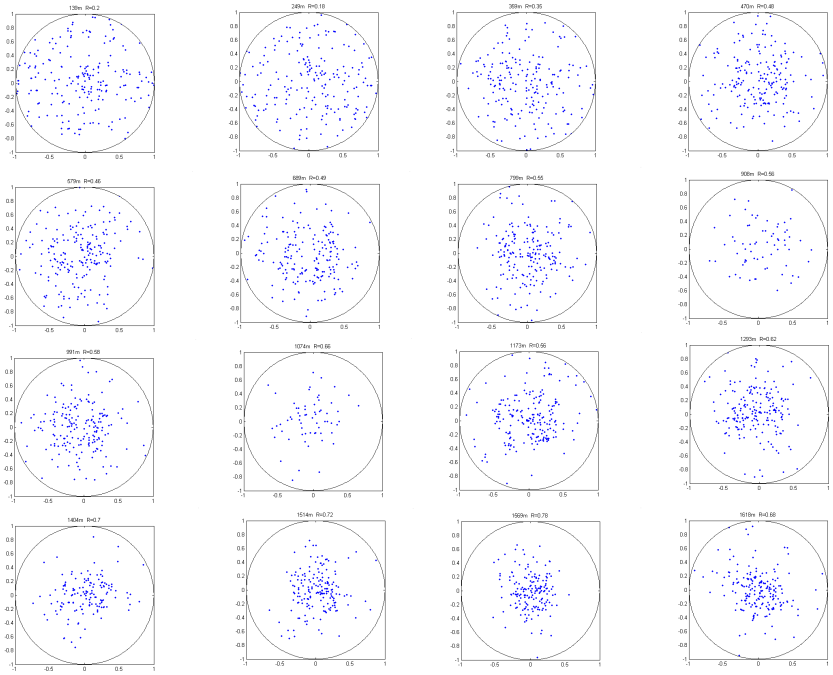

Figure A.1: *GRIP fabrics from 139 - 249 - 359 - 470 - 579 - 689 - 799 - 908 - 991 - 1074 - 1173 - 1293 - 1404 - 1514 - 1569 - 1618 m.*

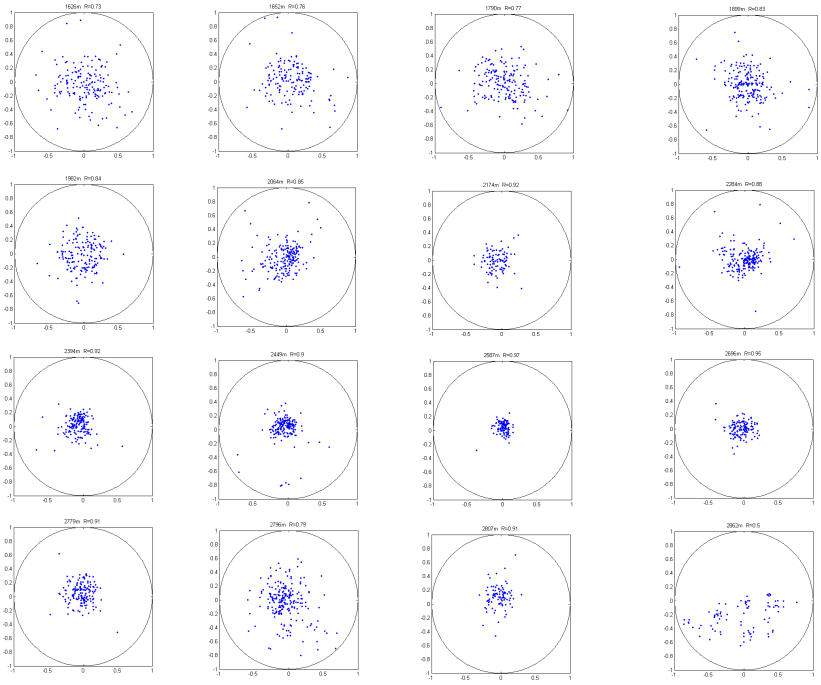

Figure A.2: *GRIP fabrics from 1652 - 1790 - 1899 - 1982 - 2064 - 2174 - 2284 - 2394 - 2449 - 2587 - 2696 - 2779 - 2796 - 2807 - 2862 m.*

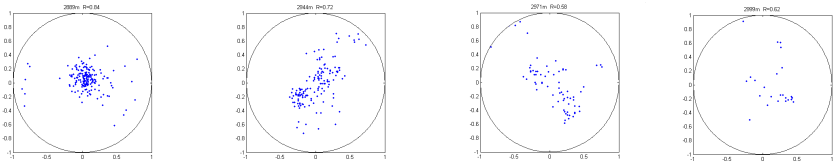

Figure A.3: *GRIP fabrics from 2889 - 2944 - 2971 - 2999 m.*

Bibliography

[Ahlmann, 1935] Ahlmann, H. (1935). Contribution to the physics of glaciers. *Geographical journal*, 86:97–113.

[Alley, 1992] Alley, R. (1992). Flow-law hypothesis for ice-sheet modeling. *Journal of Glaciology*, 38(129):245–256.

[Alley et al., 1986] Alley, R., Perepezko, J., and Bentley, C. (1986). Grain growth in polar ice: I. Theory. *Journal of Glaciology*, 32(112):10.

[Benson, 1961] Benson, C. (1961). Stratigraphic studies in the snow and firn of the Greenland Ice Sheet. *Folia Geographica Danica*, 9:13–37.

[Bjerrum, 1951] Bjerrum, N. (1951). Structure and properties of ice. *Kongelige Danske Videnskabernes Selskab Matematisk-fysiske Meddelelser*, 27:1–56.

[Castelnau et al., 1998] Castelnau, O., Shoji, H., Mangeney, A., Milsch, H., Duval, P., Miyamoto, A., Kawada, K., and Watanabe, O. (1998). Anisotropic behavior of GRIP ices and flow in Central Greenland. *Earth and Planetary Science Letters*, 154:307–322.

[Craig, 1961] Craig, H. (1961). Isotopic variations in meteoric waters. *Science*, 133:1702–1703.

[Dahl-Jensen et al., 2002] Dahl-Jensen, D., Gundestrup, N., Miller, H., Watanabe, O., Johnsen, S., Steffensen, J., ans A. Svensson, H. C., and Larsen, L. (2002). The NorthGRIP deep drilling programme. *Annals of Glaciology*, 35:1–4.

[Dansgaard et al., 1993] Dansgaard, W., Johnsen, S., Clausen, H., Dahl-Jensen, D., Gundestrup, N., Hammer, C., Hvidberg, C., Steffensen, J., Sveinbjörnsdottir, A., Jouzel, J., and Bond, G. (1993). Evidence for general instability of past climate from 250-kyr ice-core record. *Letters to nature*, 364:218–220.

[Durand et al., 2005] Durand, G., Gagliardini, O., Thorsteinsson, H., Svensson, A., Kipfstuhl, J., and Dahl-Jensen, D. (2005). Ice microstructure and fabric: an up to date approach to measure textures. *Submitted to Journal of Glaciology*, page 32.

[Durand et al., 2004] Durand, G., Graner, F., and Weiss, J. (2004). Deformation of grain boundaries in polar ice. *Europhysics Letters*, 67(6):1038–1044.

[Duval et al., 2000] Duval, P., Arnaud, L., Brissaud, O., Montagnat, M., and Chapelle, S. D. L. (2000). Deformation and recrystalllization processes of ice from polar ice-sheets. *Annals of Glaciology*, 30:83–87.

[Duval and Castelnau, 1995] Duval, P. and Castelnau, O. (1995). Dynamic Recrystallization of Ice in Polar Ice Sheets. *Journal de Physique IV*, 5(C):197–205.

[Friedel, 1964] Friedel, J. (1964). *Dislocations*. Pergamon, Oxford.

[Gagliardini et al., 2004] Gagliardini, O., Durand, G., and Wang, Y. (2004). Grain area as a statistical weight for polycrystal constituents. *Journal of Glaciology*, 50(168):87–95.

[Gow, 1969] Gow, A. (1969). On the rates of growth of grains and crystals in south polar firn. *Journal of Glaciology*, 8:241–252.

[Gow, 1994] Gow, A. (1994). Post-drilling recrystallization of the Byrd Station deep ice core and its relevance to current and future deep-core drilling on polar ice sheets. *Annals of Glaciology*, 20:231–236.

[Hansen, 2001] Hansen, K. (2001). Texture and fabrics of ice crystals in the grip ice core - a detailed study of glacial interstadial 3. Master's thesis, N.B.I. University of Copenhagen, Denmark.

[Hansen et al., 2002] Hansen, K. M., Svensson, A., Wang, Y., and Steffensen, J. (2002). Properties of GRIP ice crystals from around Greenland interstadial 3. *Annals of Glaciology*, 35:7.

[Hobbs, 1974] Hobbs, P. (1974). *Ice Physics*. Oxford University Press.

[Johnsen, 2002] Johnsen, S. (2002). The Greenland ice core records. *ESF-HOLIVAR workshop*.

[Kamb, 1972] Kamb, W. (1972). Experimental recrystallization of ice under stress. *Geophysical Monograph*, 16:211–241.

[Kossevich, 1999] Kossevich, A. (1999). *The Crystal Lattice*. WILEY-VCH.

[Langway C.C., 1968] Langway C.C., J. (1968). Ice Fabrics and the Universal Stage. *SIPRE Technical Report*, 62.

[Libbrecht, 2005] Libbrecht, K. (2005). The physics of snow crystals. *Reports on Progress in Physics*, 68:855–895.

[Lliboutry, 1965] Lliboutry, L. (1965). *Traité de Glacilogie*. Masson, Paris.

[Müller, 1962] Müller, F. (1962). Zonation in the accumulation area of the glaciers of axel heiberg island, n.w.t., canada. *Journal of Glaciology*, 4:302–313.

[North Greenland Ice Core Project Members, 2004] North Greenland Ice Core Project Members (2004). High-resolution record of Northern Hemisphere climate extending into the last interglacial period. *Nature*, 431:4.

[Paterson, 1994] Paterson, W. (1994). *The Physics of Glaciers*.

[Petrenko and Whitworth, 2002] Petrenko, V. and Whitworth, R. (Mar 1, 2002). *Physics of Ice*. Oxford University Press.

[Pnevmatikos, 1988] Pnevmatikos, S. (1988). Soliton Dynamics of Hydrogen-Bonded Networks: A mechanism for Proton Conductivity. *Physical Review Letters*, 60(15):1534–1537.

[Poirier, 1985] Poirier, J.-P. (1985). *Creep of Crystals*. Cambridge University Press.

[Riege et al., 1998] Riege, S., Thompson, C., and Frost, H. (1998). The effect of particle pinning on grain size distributions in 2D simulations of grain growth, in Grain Growth in Polycrystalline Materials III, edited by H. Weiland, B.L. Adams and A.D. Rollet. *Metals and Mater*, pages 295–301.

[Schulz, 2002] Schulz, M. (2002). On the 1470-year pacing of Dansgaard-Oeschger warm events. *Paleoceanography*, 17(2):4–1 / 4–9.

[Svensson et al., 2003a] Svensson, A., Baadsager, P., Persson, A., Hvidberg, C., and Siggaard-Andersen, M. (2003a). Seasonal stability in ice crystal properties at NorthGRIP: a case of study around 301 m depth. *Annals of Glaciology*, 37:4.

[Svensson et al., 2005] Svensson, A., Nielsen, S., Kipfstuhl, S., Johnsen, S., Steffensen, J., Bigler, M., Ruth, U., and Röthlisberger, R. (2005). Visual stratigraphy of the North Greenland Ice Core Project (NorthGRIP) ice core during the last glacial period. *Journal of Geophysical Research*, 110(D02108).

[Svensson et al., 2003b] Svensson, A., Schmidt, K., Dahl-Jensen, D., Johnsen, S., Wang, Y., Kipfstuhl, S., and Thorsteinsson, T. (2003b). Properties of ice crystals in northgrip late- to middle-holocene ice. *Annals of Glaciology*, 37:6.

[Thorsteinsson, 1996] Thorsteinsson, T. (1996). *Textures and fabrics in the GRIP ice core, in relation to climate history and ice deformation*. PhD thesis, Alfred Wegener Institue for Polar and Marine Research - University of Bremerhaven (Germany).

[Thorsteinsson et al., 1997] Thorsteinsson, T., Kipfstuhl, J., and Miller, H. (1997). Textures and fabrics in the GRIP ice core. *Journal of geophysical research*, 102(C12):26,586–26,599.

[Wang et al., 2002] Wang, Y., Thorsteinsson, T., Kipfstuhl, J., Miller, H., Dahl-Jensen, D., and Shoji, H. (2002). A vertical girdle fabric in the NorthGRIP deep ice core, North Greenland. *Annals of Glaciology*, 35:6.

[Weertman and Weertman, 1964] Weertman, J. and Weertman, J. (1964). Elementary Dislocation Theory. *Macmillan*, 81.

[Weiss et al., 2002] Weiss, J., Vidot, J., Gay, M., Arnaud, L., Duval, P., and Petit, J. (2002). Dome Concordia ice microstructure: impurities effect on grain growth. *Annals of Glaciology*, 35:552–558.

[Woodcock, 1977] Woodcock, N. (1977). Specification of fabric shapes using an eigenvalue method. *GSA Bulletin*, 88(9):1231–1236.